

Research Paper

Diffuse galaxy cluster emission at 168 MHz within the Murchison Widefield Array Epoch of Reionization 0-hour field

S. W. Duchesne^{1,2*}, M. Johnston-Hollitt^{2,3}, A. R. Offringa⁴, G. W. Pratt⁵, Q. Zheng^{6,7} and S. Dehghan¹

¹School of Chemical and Physical Sciences, Victoria University of Wellington, P. O. Box 600, Wellington 6140, New Zealand

²International Centre for Radio Astronomy Research (ICRAR), Curtin University, Bentley, WA 6102, Australia

³Curtin Institute for Computation, Curtin University, GPO Box U1987, Perth, WA 6845, Australia

⁴Netherlands Institute for Radio Astronomy (ASTRON), PO Box 2, NL-7990 AA Dwingeloo, the Netherlands

⁵AIM, CEA, CNRS, Université Paris-Saclay, Université Paris Diderot, Sorbonne Paris Cité, F-91191 Gif-sur-Yvette, France

⁶School of Engineering and Computer Science, Victoria University of Wellington, PO Box 600, Wellington 6140, New Zealand

⁷Shanghai Astronomical Observatory, Chinese Academy of Sciences, 80 Nandan Road, Shanghai 200030, China

Abstract

We detect and characterise extended, diffuse radio emission from galaxy clusters at 168 MHz within the Epoch of Reionization 0-hour field: a $45^\circ \times 45^\circ$ region of the southern sky centred on R. A. = 0° , decl. = -27° . We detect 29 sources of interest; a newly detected halo in Abell 0141; a newly detected relic in Abell 2751; 4 new halo candidates and a further 4 new relic candidates; and a new phoenix candidate in Abell 2556. Additionally, we find 9 clusters with unclassifiable, diffuse steep-spectrum emission as well as a candidate double relic system associated with RXC J2351.0-1934. We present measured source properties such as their integrated flux densities, spectral indices (α , where $S_\nu \propto \nu^\alpha$), and sizes where possible. We find several of the diffuse sources to have ultra-steep spectra including the halo in Abell 0141, if confirmed, showing $\alpha \leq -2.1 \pm 0.1$ with the present data making it one of the steepest-spectrum haloes known. Finally, we compare our sample of haloes with previously detected haloes and revisit established scaling relations of the radio halo power ($P_{1.4}$) with the cluster X-ray luminosity (L_X) and mass (M_{500}). We find that the newly detected haloes and candidate haloes are consistent with the $P_{1.4}$ - L_X and $P_{1.4}$ - M_{500} relations, and see an increase in scatter in the previously found relations with increasing sample size likely caused by inhomogeneous determination of $P_{1.4}$ across the full halo sample. We show that the MWA is capable of detecting haloes and relics within most of the galaxy clusters within the *Planck* catalogue of Sunyaev-Zel'dovich sources depending on exact halo or relic properties.

Keywords: radio continuum: general – galaxies: clusters: general – radiation mechanisms: non-thermal – galaxies: clusters: individual: (Abell 0033, Abell 0141, Abell 2811, Abell S1121, Abell 2751, Abell 2556, Abell S1136, Abell 0122, RXC J2351.0-1934)

1. Introduction

Clusters of galaxies are among the largest structures in the Universe. Understanding how clusters form and their dynamics is key to understanding how the Universe behaves on some of the largest scales. Galaxy clusters are thought to form in the hierarchical model, where galaxies eventually clump together during sometimes intense merger events (Peebles, 1980). The clusters themselves are primarily dark matter, diffuse gas that makes up the intra-cluster medium (ICM), and the galaxies for which they are named. Galaxy clusters are found to host magnetic fields on the order of 0.1–1 μG (Clarke et al., 2001; Johnston-Hollitt, 2003; Bonafede et al., 2010). The magnetic fields in clusters give rise to radio synchrotron emission; relativistic electrons accelerated by the magnetic fields with Lorentz factors of $\gamma > 1000$, where the spectral energy distribution (SED) of the emission gives insight into the ages of electron populations and the possible shock-driven re-acceleration from merger events (see Feretti et al., 2012; Brunetti & Jones, 2014; van Weeren et al., 2019,

for reviews). The steep spectral indices¹ of such synchrotron emission means that to detect the faintest non-thermal diffuse cluster emission low-frequency radio telescopes are required, such as the Giant Metrewave Radio Telescope (GMRT; Ananthakrishnan, 1995), the Murchison Widefield Array (MWA; Tingay et al., 2013), and the LOw Frequency ARray (LOFAR; van Haarlem et al., 2013). As radio telescopes become more sensitive, more of this steep-spectrum diffuse emission is expected to be found (Cassano et al., 2012; Johnston-Hollitt, 2017).

Diffuse synchrotron emission comes in two main classes: cluster haloes and relics. Cluster relics can be broken down further into two types: kpc-scale *phoenixes* and *megaparsec-scale relics*. The kpc-scale radio phoenixes are thought to be emission from revived fossil plasma left over from long dormant radio galaxies (see e.g. Enßlin & Gopal-Krishna, 2001; Enßlin & Brüggen, 2002) and are usually found near the cluster centre (e.g. Slee et al., 2001). Megaparsec-scale

*email: stefan.duchesne.astro@gmail.com

¹The spectral index α is defined through $S_\nu \propto \nu^\alpha$ for flux density S_ν at frequency ν .

relics (hereafter relics) are thought to trace shocks through the ICM during and after massive merger events. These are found on the periphery of clusters, usually aligned with the major merger axis and can come in adjacent pairs of so-called *double relics* (e.g. Abell 3667; Johnston-Hollitt 2003, Abell 3376; Bagchi et al. 2006, PSZ1 G108.18–11.53; de Gasperin et al. 2015). For both types of relics the electrons must go through some re-acceleration process albeit on vastly different scales. These processes are thought to be through shocks typically resulting in an elongated or arc-like morphology in the case of relics. The key observed distinction between the two types of emission are their size and spectral properties. Phoenixes, thought to form through adiabatic shock compression, can show curved spectra (Enßlin & Gopal-Krishna, 2001) whereas relic spectra typically resemble power laws (e.g. Hindson et al., 2014; George et al., 2017; Rajpurohit et al., 2020).

Haloës also come in two main types: *mini-haloës* and *cluster haloës*. Mini-haloës are associated with strong active galactic nuclei (AGN), often the central dominant (cD) galaxy within the core of the cluster, and are smaller in extent though are otherwise morphologically similar to cluster haloës (for a recent review see Bravi et al., 2016). Cluster haloës are centrally located within the cluster, morphologically regular, and are often found to coincide with the X-ray emitting plasma of the ICM. Haloës do not normally show any significant fractional polarisation however this is likely a limitation of the resolution of current-generation radio interferometers (Govoni et al., 2013). The mechanism that generates these radio haloës is still under investigation. The primary, re-acceleration model of halo generation suggests the synchrotron emission occurs after electrons are re-accelerated through merger-driven turbulence in the magnetised ICM (see e.g. Brunetti et al., 2001; Buote, 2001; Petrosian, 2001; Petrosian & East, 2008; Cassano et al., 2012). An alternate model is that of hadronic origin (see e.g. Dennison, 1980; Dolag & Enßlin, 2000). In this secondary model, electrons are generated as secondary products of collisions between cosmic ray protons and ICM protons. Pions, a product in these proton-proton collisions, produce the electrons that will be accelerated by magnetic fields, as well as γ -rays. This model not only requires γ -ray emission from clusters, but also that all galaxy clusters host radio haloës at some level. The synchrotron emission from electrons produced through these proton-proton collisions will be significantly weaker than that seen through re-acceleration via turbulence (Blasi & Colafrancesco, 1999). So far only upper limits for γ -ray emission have been presented (e.g. Ackermann et al., 2014; Prokhorov & Churazov, 2014; Liang et al., 2016), and with current generation radio telescopes, the necessary sensitivity to detect haloës generated through the secondary model alone has not been reached. The primary and secondary models are not mutually exclusive, and there has been work to combine the two models (e.g. Brunetti & Blasi, 2005; Brunetti & Lazarian, 2011, 2016). The primary model is observationally supported by the fact that predominantly unrelaxed, X-ray

luminous clusters are known to host radio haloës. However radio halo detection had been biased toward those clusters hosting highly X-ray luminous plasma as these are the clusters often targeted (e.g. Giovannini et al., 1999; Venturi et al., 2007, 2008; Kale et al., 2013, 2015). Only recently have surveys been conducted to search for diffuse cluster emission without preselecting clusters based solely on their X-ray luminosities. For example, Bernardi et al. (2016) select clusters based on mass, and Shakouri et al. (2016) survey clusters over a wide range of X-ray luminosities.

Given the comparative rarity of diffuse cluster emission detection, we wish to perform larger surveys to properly ascertain the incidence and nature of these types of radio emission. In this paper we present the results of one such survey using a deep $45^\circ \times 45^\circ$ image produced by the MWA as part of the MWA Epoch of Reionization (EoR) project (Bowman et al., 2013; Offringa et al., 2016). This study forms the pilot for a larger search for diffuse cluster emission (Johnston-Hollitt et al. in prep.) using the recently released GaLactic and Extragalactic All-sky MWA survey (GLEAM; Wayth et al., 2015), which covers the entire southern sky below a declination of $+25^\circ$ and covers the frequency range 72–231 MHz. In the following sections we discuss the various images used and the process involved in searching for diffuse cluster emission.

This paper unless otherwise stated assumes a flat Λ CDM cosmology with $H_0 = 70 \text{ km s}^{-1} \text{ Mpc}^{-1}$, $\Omega_M = 0.3$, and $\Omega_\Lambda = 1 - \Omega_M$.

2. The search for diffuse cluster emission

2.1. The Epoch of Reionization 0-hour field

As part of the MWA EoR project Offringa et al. (2016) present a $45^\circ \times 45^\circ$ image centred on $(\alpha_{J2000}, \delta_{J2000}) = (00^{\text{h}}00^{\text{m}}00^{\text{s}}, -27^\circ00'00'')$, at a frequency of 168 MHz called the EoR0 field. This image is obtained from 45 hours of integration and has a resolution of 2.3 arcmin. The EoR0 field is the deepest, confusion limited image made with the 128-tile Phase I MWA². In addition to the overall sensitivity, the low surface brightness imaging capability provided by the number of short ($\leq 60 \text{ m}$) baselines makes the MWA a powerful tool to investigate extended, diffuse emission. Data collection, reduction, and imaging for the field used here is explained in detail in Offringa et al. (2016). Whilst the primary purpose of the EoR0 field is the study of EoR, the image itself is incredibly sensitive for an MWA image at this frequency, reaching down to $\sim 2.3 \text{ mJy beam}^{-1}$ near the centre of the image and increasing up to $\sim 100 \text{ mJy beam}^{-1}$ out towards the image edges. This surface brightness sensitivity makes the EoR0 field useful in the search for steep spectrum cluster haloës and relics. The R.A. and decl. range used here is as follows: $(22^{\text{h}}29^{\text{m}}55^{\text{s}}.2 \leq \alpha_{J2000} \leq 01^{\text{h}}29^{\text{m}}57^{\text{s}}.6)$ and $(-44^\circ41'24'' \leq \delta_{J2000} \leq -08^\circ36'36'')$, which is chosen to cut out the most significant noise at the edge of the image.

²Since this work was undertaken the MWA has been upgraded to the so-called Phase II MWA (see Wayth et al. 2018 for details).

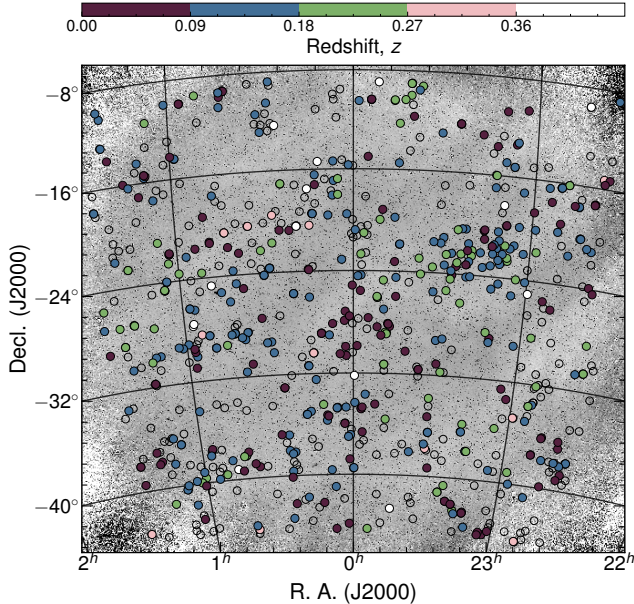


Figure 1. The central $\sim 42^\circ$ of the Epoch of Reionization 0-hour field. Overlaid are the positions of galaxy clusters from the (Abell et al., 1989) catalogues, MCXC, and the PSZ1. We cut the sample of clusters in an attempt to avoid the edges of the image where the noise is highest. The filled circles are coloured according to their redshift. Unfilled circles are those without a measured redshift. Note the side-lobe structure of the primary beam appearing in the corners of the image. The colourmap of the redshift distribution is an implementation of cubeheLiX (Green, 2011).

2.2. Catalogues of galaxy clusters

Within the EoR0 field we searched for diffuse emission within a ~ 2 Mpc radius around clusters within the following catalogues: Abell revised North, South, and Supplementary catalogues (Abell et al., 1989, hereafter ACO, but see also Abell 1958); the Meta-Catalogue of X-ray detected Clusters of galaxies (Piffaretti et al., 2011, hereafter MCXC); the *Planck* catalogue of Sunyaev–Zel’dovich sources (Planck Collaboration et al., 2015, hereafter PSZ1)³. Within the region encompassed by the EoR0 field, and excluding those clusters that lie too far to the edge of the image, this constitutes 668 unique clusters, 505 unique to ACO, 70 unique to MCXC, and 19 unique to PSZ1, with 24 clusters present in all three catalogues. Fig. 1 shows the distribution of ACO, PSZ1, and MCXC clusters within the EoR0 field, coloured by redshift where available.

All clusters are checked systematically for diffuse cluster emission except 217 clusters in the ACO catalogue without a redshift. For clusters without a redshift we are unable to determine the projected linear distance from the cluster centre, which makes determining if emission is part of the cluster difficult if not at the centre. Whilst this does not pose much problem for haloes, we also consider that ACO clusters without a redshift are unlikely to have auxiliary data in the form of cluster mass, X-ray luminosities, or information on

cluster members. Further, cluster emission serendipitously found in clusters not part of the aforementioned catalogues is investigated when noticed.

2.3. Source detection and measurement

2.3.1. Manual source-finding: eyeballing galaxy clusters

While source-finding algorithms exist and are put to good use to produce point-source catalogues, automated source-finding can miss the extended, low surface brightness haloes and relics within clusters (Hollitt & Johnston-Hollitt, 2012). Therefore the EoR0 field is searched by eye for diffuse emission. Auxiliary radio data exists in the form of the following sky surveys: the NRAO VLA Sky Survey⁴ (NVSS; Condon et al., 1998), the Sydney University Molonglo Sky Survey (SUMSS; Bock et al., 1999; Mauch et al., 2003), the TFIR⁵ GMRT Sky Survey (alternate data release, TGSS; Intema et al., 2017), and the VLA Low-frequency Sky Survey redux (VLSSr; Lane et al., 2014). These surveys and their salient properties are summarised in Table 1. Beyond radio surveys, we use the *Röntgen SATellite* (ROSAT; Trümper, 1984) All-Sky Survey (RASS; Voges et al., 1999), the Digitized Sky Survey (DSS2), the first Pan-STARRS⁶ survey—PS1 (Tonry et al., 2012; Chambers et al., 2016), the Dark Energy Survey Data Release 1 (DES DR1; Abbott et al., 2018; Morganson et al., 2018; Flaugher et al., 2015), as well as archival *Chandra* data with the Advanced CCD Imaging Spectrometer (ACIS) instrument and *XMM-Newton* data with the European Photon Imaging Camera (EPIC) instrument, where available. For a small selection of clusters, we utilise deep (> 30 ks exposure) X-ray images from the Representative *XMM-Newton* Cluster Structure Survey (REXCESS; Böhringer et al., 2007; Pratt et al., 2009).

To determine the nature of detected emission, we look for the following:

- i. high-frequency counterparts (1.4 GHz and 843 MHz),
- ii. low-frequency counterparts (147.5 and 74 MHz),
- iii. optical identifications, and
- iv. X-ray emission coincident with centrally located radio emission.

(i) and (ii) are used as an easy method of checking if we are looking at blended point sources. (i) gives a quick insight into the spectral index of the source, with significant high frequency emission, at least comparably to 168 MHz, a flat spectral index is present which is uncharacteristic of diffuse cluster emission. (iii) is important as cluster haloes and relics are not associated with an optically visible galaxy, though in the case of cluster haloes there is expected to be a concentration of optically visible galaxies due to the central location in the cluster. If an optically visible galaxy is found at the

⁴National Radio Astronomy Observatory Very Large Array Sky Survey

⁵Tata Institute of Fundamental Research.

⁶Panoramic Survey Telescope And Rapid Response System; Kaiser et al. 2010.

³Note that PSZ2 was not available when this work was started.

Table 1 Existing sky surveys used as auxiliary data to the EoR0 field.

Survey	Frequency MHz	Declination (J2000, °)	Resolution ^a (arcsec × arcsec)	σ_{rms} (mJy beam ⁻¹)
EoR0 field	168	$-44^{\circ}41'24'' \leq \delta \leq -08^{\circ}36'36''$	138×138	$\gtrsim 2.3$
NVSS	1400	≥ -40	45×45	$\gtrsim 0.45$
SUMSS	843	≤ -30	$\sim 2.2 (45 \times 45)$	$\gtrsim 2$
TGSS	147.5	$\gtrsim -53$	$\sim 1.5 (25 \times 25)$	$\gtrsim 3.5$
VLSSr	74	≥ -30	75×75	$\gtrsim 100$

^a At $\delta_{\text{J2000}} = -27^{\circ}$.

peak of the diffuse emission or between two lobes, then the likelihood is that of extended, disturbed, or otherwise normal lobes of a radio galaxy. (iv) allows us to confidently classify centrally located diffuse emission as a cluster halo or relic. In particular, *Chandra* or *XMM-Newton* observations are detailed enough to provide the position and any elongation of the X-ray emission relative to any centrally located diffuse radio emission. With these points forming the foundations of our search, we eyeballed the subset of clusters described in Section 2.2, followed by measurements of relevant physical properties.

2.3.2. Local noise properties

The EoR0 field is a large image that has greatly varying rms noise throughout. However, corners of the image feature significant noise due to the primary beam null. Offringa et al. (2016) use *bane*⁷ (Hancock et al., 2012) to estimate noise throughout the EoR0 field. The mean noise level is calculated to be 3.2 ± 0.6 mJy beam⁻¹ for the central 10° of the image. Large-scale diffuse structure of Galactic origin is seen streaking the image which leads to non-constant background signal affecting rms noise calculations. In regions with no Galactic emission the rms can be as low as ~ 2 mJy beam⁻¹. Additionally, typical local rms noise values for the various survey data are provided in Table 1.

2.3.3. Integrated flux densities

The software that generated the EoR0 field at the time did not calculate a correct synthesized beam for the restored, stacked image. As a result, the integrated flux densities measured directly from the image are incorrect. We find that the integrated flux density measurements of the EoR0 field differed by a systematic factor of approximately 30% when compared to the nearly equivalent 162–170 MHz band in the GLEAM survey which is tied to the Baars flux scale (Baars et al., 1977).

To scale the integrated flux densities in the EoR0 field we choose six reasonably bright (> 2 Jy) unresolved sources, exhibiting no side-lobe structure and no blending with nearby sources. From a linear fit between the GLEAM 162–170 MHz and EoR0 168 MHz flux densities we find a factor 0.69 ± 0.05

to be used for calibration of measured integrated flux densities (i.e., $S_{168, \text{corrected}} = 0.69 \times S_{168}$), and this calibration is used through the remainder of this paper.

Flux densities of extended sources are either calculated by purpose-built `fluxtools.py`⁸ code or by using `aegean` if sources are blended, as the aforementioned `python` code does not fit sources, and assumes each source is discrete. Both methods measure the source flux densities down to the $2.6\sigma_{\text{rms}}$ level so as to include as much real contribution from the faint sources as possible (e.g. Kapińska et al., 2017, but see also Hales et al. 2012). We do not use `aegean` for all sources as `aegean` is intended as a point-source-finder, and will give the best results measuring such sources. Each flux measurement has an uncertainty, σ_{S_v} , calculated as

$$\sigma_{S_v} = \sqrt{S_v^2 (\sigma_{\text{scale}}^2 + \sigma_{\text{rescale}}^2) + \left(\sigma_{\text{rms}} \sqrt{N_{\text{beam}}} \right)^2} \quad [\text{Jy}], \quad (1)$$

where N_{beam} is the number of beams crossing the extended source, $\sigma_{\text{scale}} = 5\%$ —the flux scale error as described in Section 4.1 of Offringa et al. (2016), and $\sigma_{\text{rescale}} = 5\%$ for the additional uncertainty in rescaling the integrated flux density measurements. The last term is the standard error given to flux density measurements of extended sources.

2.3.4. Spectral indices and source sizes

Where possible a spectral index is calculated for each source assuming the SED follows a standard power law in the relevant frequency range. This is either done as a two-point spectral index ($\alpha = \ln(S_1/S_2) / \ln(\nu_1/\nu_2)$) or by fitting a first-order polynomial to the flux density measurements in log-log space, hence fitting a power law to the data. Over the frequency range here (74–1400 MHz) haloes and relics tend not to show any turnovers or breaks and typically do not deviate from the assumed power law except in rare instances (e.g. the relic in Abell 2443 which has a break near 325 MHz reported by Cohen & Clarke, 2011). Phoenixes, however, can show curved spectra (e.g. Slee et al., 2001; Kale & Dwarakanath, 2012). For the purpose of this work (and often in the absence of more than two flux density measurements) we assume power laws model these SEDs sufficiently

⁷<https://github.com/PaulHancock/Aegean/wiki/BANE>

⁸<https://gist.github.com/Sunmish/198ef88e1815d9ba66c0f3ef3b18f74c>

Table 2 Details of the 2.1-GHz ATCA observations of Abell S1063.

Array	Date	t_{scan} (min)	θ_{max} ^a (arcmin)
EW352	2013 Jun 18,20,22	224	19.6
6A	2012 Feb 3–5	543	1.8

^a Maximum angular scale sensitivity.

in the relevant frequency regime as is often the case (see e.g. Abell 0013; George et al., 2017).

Where appropriate, we estimate limits to flux densities. In particular, we use this for estimating 1.4 GHz and 147.5 MHz limits when 168 MHz emission has no counterpart in the NVSS or TGSS survey images, respectively. These are used then to impose limits on the spectral indices. For such sources, we estimate the source area at 168 MHz, which is a function of the MWA beam at $B_{\text{maj}} \approx 2.3$ arcmin, and attempt to correct for the difference in beam sizes between the VLA (NVSS), GMRT (TGSS), and MWA (EoR0) by naively taking the ratios of B_{maj} and correcting the area based on this ratio. The limit is then

$$S_{\text{limit}} = \sigma_{\text{rms}} f A_{168} \times \frac{4 \ln 2}{\pi B_{\text{maj}} B_{\text{min}}} \quad [\text{Jy}], \quad (2)$$

where $f = B_{\text{maj}}/B_{\text{maj},168}$ and A_{168} is the source area measured at 168 MHz.

A largest-angular size/scale (LAS) is provided where possible. For extended sources that are confused and blend with nearby sources, we estimate an angular size by making an assumption on how far the diffuse source has blended into any nearby point sources. The size characterisation is important to determine if the detection is truly extended. For a non-blended source to be considered extended in this work it must have an LAS that is greater than $1.5 B_{\text{maj}}$, where $B_{\text{maj}} \approx 2.3$ arcmin, which is approximately the expected B_{maj} of the EoR0 field. Finally, any measured angular scale is deconvolved from the beam size before a linear project size is calculated, and we report on the deconvolved sizes only.

2.4. Additional Australia Telescope Compact Array observations

One cluster, Abell S1063, had unpublished archival Australia Telescope Compact Array (ATCA; Frater et al., 1992) observations made with the Compact Array Broadband Backend (CABB; Wilson et al., 2011). The cluster was observed in two array configurations: EW352 (Project code C2837, PI: M. Johnston-Hollitt) and 6A (Project code C2585, PI: R. Kale), and the data were retrieved from the Australia Telescope Online Archive. Table 2 summarises the properties of the observations.

The reduction of ATCA data follows standard procedures of continuum data reduction with *miriad*. After radio frequency interference flagging, flux and bandpass calibration

Table 3 Sub-band image properties for the ATCA observations of Abell S1063.

Image	ν_c ^a (MHz)	Restoring beam ($'' \times ''$, $^\circ$)	σ_{rms} ($\mu\text{Jy beam}^{-1}$)
1332	1384	9.95×4.45 , -3.1	50
1844	1873	7.57×3.89 , 1.5	21
2356	2349	6.10×3.15 , 0.0	22
2868	2811	5.13×2.74 , -4.0	26
Stacked	2034	9.95×4.45 , -3.1	18
Stacked ^b	2251	122.9×40.1 , -17.7	360

^a Effective central frequency of image.^b Stacked after tapering sub-bands with a 60 arcsec Gaussian.

with PKS B1934–638, gain and phase calibration is performed with PKS B2326–477 and MRC 2117–614 for the EW352 and 6A configurations, respectively. Imaging is performed with the multi-frequency CLEAN task *mfclean* with a ‘Briggs’ (Briggs, 1995) *robust = 0.0* image weighting after splitting the data into 512 MHz subbands. Two rounds of phase-only self-calibration are performed on each subband independently. An additional stacked image is made for the full 2-GHz bandwidth, and one final tapered, stacked image is made. Table 3 summarises the image properties.

3. Results

3.1. Diffuse cluster emission at 168 MHz

Here we present the cluster emission detected in the EoR0 field from the ACO, PSZ1, and MCXC catalogues. We detect 30 objects of interest, of which 29 are candidate relics, phoenixes, or haloes associated with 25 clusters. The clusters found to host candidate diffuse emission are presented in Table 4 along with their physical properties. The detection rate for such emission within the EoR0 field is $\sim 6.4\%$, which on average is lower than previous surveys, (e.g. $\sim 32\%$: Venturi et al. 2007, 2008, $\sim 17\%$: Bernardi et al. 2016, $\sim 12\%$: Shakouri et al. 2016), however as mentioned, previous surveys target the most massive, and X-ray luminous clusters. Included are previously detected relics in Abell 0013, Abell 0085, and Abell 2744 (Slee & Reynolds, 1984; Slee et al., 2001; Govoni et al., 2001), phoenixes in Abell 0133 and Abell 4038 (Slee & Reynolds, 1984; Slee & Roy, 1998; Slee et al., 2001), haloes in Abell 2744 and MACS J2243.3–0935 (Govoni et al., 2001; Cantwell et al., 2016), as well as the large, ambiguous emission seen in Abell 0133 (Randall et al., 2010). For the purpose of distinguishing between relics and phoenixes, we place a limit of 400 kpc as a maximum size of a phoenix. Where emission scale approaches this size we look at the spectral index and location, where a linear size approaching 400 kpc with ultra-steep spectral indices ($\alpha < -1.5$, Kempner et al. 2004) and a location closer to the cluster’s centre would be suggestive of phoenixes rather than

Table 4 Select physical properties of clusters found to host diffuse emission.

Cluster name	α_{J2000}	δ_{J2000}	z	M_{500} ($\times 10^{14} M_{\odot}$)	$L_{X,500}$ ($\times 10^{44} \text{ erg s}^{-1}$)	References
Abell 0013	00 ^h 13 ^m 38 ^s .3	-19°30'07"	0.0940	2.79 ^{+0.36} _{-0.38}	1.236	(a)/(b)/(c)/(b)
Abell 0022	00 ^h 20 ^m 42 ^s .8	-25°42'37"	0.1424	4.56 ^{+0.42} _{-0.44}	2.872	(a)/(d)/(c)/(b)
Abell 0033	00 ^h 27 ^m 07 ^s .0	-19°30'24"	0.2395	-	-	(a)/(e)/-/-
Abell 0085	00 ^h 41 ^m 50 ^s .1	-09°18'06"	0.0551	4.90 ^{+0.21} _{-0.22}	5.100	(a)/(f)/(c)/(b)
Abell 0122	00 ^h 57 ^m 24 ^s .7	-26°16'50"	0.1135	1.727	0.861	(a)/(g)/(b)/(b)
Abell 0133	01 ^h 02 ^m 42 ^s .1	-21°52'25"	0.0562	3.08 ^{+0.23} _{-0.24}	1.460	(a)/(h)/(c)/(b)
Abell 0141	01 ^h 05 ^m 34 ^s .8	-24°39'16"	0.230	4.48 ^{+0.66} _{-0.73}	5.161	(a)/(i)/(c)/(b)
Abell 2496	22 ^h 51 ^m 00 ^s .6	-16°24'24"	0.1221	2.98 ^{+0.41} _{-0.44}	2.031	(a)/(b)/(c)/(b)
Abell 2554	23 ^h 12 ^m 20 ^s .7	-21°30'02"	0.1108	3.05 ^{+0.37} _{-0.39}	1.431	(a)/(j)/(c)/(b)
Abell 2556	23 ^h 13 ^m 00 ^s .9	-21°37'54"	0.0871	2.476	1.509	(a)/(j)/(b)/(b)
Abell 2680	23 ^h 56 ^m 28 ^s .3	-21°02'17"	0.1771	-	-	(a)/(e)/-/-
Abell 2693	00 ^h 02 ^m 09 ^s .6	-19°33'17"	0.173	-	-	(a)/(k)/-/-
Abell 2721	00 ^h 06 ^m 03 ^s .0	-34°43'27"	0.1144	3.77 ^{+0.35} _{-0.37}	1.810	(a)/(g)/(c)/(b)
Abell 2744	00 ^h 14 ^m 18 ^s .9	-30°23'21"	0.3066	9.56 ^{+0.49} _{-0.51}	11.818	(a)/(b)/(c)/(b)
Abell 2751	00 ^h 16 ^m 19 ^s .8	-31°21'55"	0.107	1.261	0.495	(a)/(i)/(b)/(b)
APMCC 039	00 ^h 17 ^m 37 ^s .6	-31°28'14"	0.082	-	-	(l)/(l)/-/-
Abell 2798	00 ^h 37 ^m 27 ^s .0	-28°31'52"	0.105	1.315	0.546	(a)/(i)/(b)/(b)
Abell 2811	00 ^h 42 ^m 08 ^s .7	-28°32'08"	0.1079	3.67 ^{+0.35} _{-0.37}	2.734	(a)/(g)/(c)/(b)
Abell 4038	23 ^h 47 ^m 43 ^s .2	-28°08'29"	0.0282	2.038	1.030	(a)/(m)/(b)/(b)
Abell S0084	00 ^h 49 ^m 24 ^s .0	-29°31'27"	0.1080	2.368	1.438	(a)/(g)/(b)/(b)
Abell S1099	23 ^h 13 ^m 15 ^s .7	-23°08'39"	0.1104	-	-	(a)/(j)/-/-
Abell S1121	23 ^h 25 ^m 13 ^s .0	-41°12'29"	0.3580	7.05 ^{+0.61} _{-0.60}	-	(a)/(n)/(c)/-
Abell S1136	23 ^h 36 ^m 17 ^s .0	-31°36'37"	0.0625	1.289	0.504	(a)/(o)/(b)/(b)
RXC J2351.0-1954	23 ^h 51 ^m 01 ^s .4	-19°56'42"	0.2477	5.60 ^{+0.59} _{-0.62}	4.33 ± 0.84	(q)/(c)/(c)/(q)
MACS J2243.3-0935	22 ^h 43 ^m 21 ^s .5	-09°35'44"	0.447	10.07 ^{+0.58} _{-0.60}	15.200	(r)/(s)/(c)/(b)
PSZ1 G082.31-67.01	23 ^h 51 ^m 47 ^s .8	-08°58'35"	0.3939	5.90 ^{+0.78} _{-0.84}	-	(c)/(p)/(c)/-
Abell S1063	22 ^h 48 ^m 43 ^s .5	-44°31'44"	0.3475	11.41 ^{+0.43} _{-0.44}	27.167	(a)/(t)/(c)/(b)

References (catalogue/redshift/mass/X-ray luminosity): (a) [ACO](#); (b) [MCXC](#); (c) [PSZ1](#); (d) [Pimbblet et al. \(2006\)](#); (e) [Wen & Han \(2013\)](#); (f) [Oegerle & Hill \(2001\)](#); (g) [Zaritsky et al. \(2006\)](#); (h) [Way et al. \(1997\)](#); (i) [Struble & Rood \(1999\)](#); (j) [Caretta et al. \(2002\)](#); (k) [Coziol et al. \(2009\)](#); (l) [Dalton et al. \(1997\)](#); (m) [Sanders et al. \(2011\)](#); (n) [Liu et al. \(2015\)](#); (o) [Schwope et al. \(2000\)](#); (p) [Planck Collaboration et al. \(2014\)](#); (q) [Chon & Böhringer \(2012\)](#); (r) [Ebeling et al. \(2001\)](#); (s) [Ebeling et al. \(2010\)](#); (t) [Böhringer et al. \(2004\)](#).

relics. Table 5 summarises the results of the diffuse emission search. Following this, Section 3.2 describes each cluster along with the diffuse emission detected within it. Images featuring optical DSS2 backgrounds are three-colour images with red, green, and blue (RGB) corresponding to infrared, red, and blue respectively unless otherwise stated. Insets on figures are RGB images made with the PS1 (z , i , r bands) or DES DR1 (i , r , g bands) images. Radio contours in images increase with factors of 2 unless otherwise noted.

Table 5 List of diffuse emission presented in this paper, in the order presented in Section 3.2.

Cluster	Type ^a	New	α_{J2000} ^b	δ_{J2000} ^b	S_{168} (mJy)	α	LAS ^l (arcmin)	LLS ^l (kpc)
Abell 0013 ^c	R	×	00 ^h 13 ^m 28 ^s .8	−19°30′00″	1850 ± 130	$\alpha_{168}^{1400} = -1.96 \pm 0.08$	5.9	610
Abell 0022	cR or cH	✓	00 ^h 20 ^m 38 ^s .4	−25°39′36″	-	-	-	-
Abell 0033	cR of RG	✓	00 ^h 27 ^m 33 ^s .6	−19°32′24″	26 ± 5	$\alpha_{168}^{1400} \leq -0.4(\pm 0.1)$	6.3	1400 ^d
Abell 0085 ^c	P	×	00 ^h 41 ^m 31 ^s .2	−09°22′12″	9390 ± 960	$\alpha_{147.5}^{300} = -1.85 \pm 0.03$	6.7	430
Abell 0122	cmH or RG	✓	00 ^h 57 ^m 24 ^s .0	−26°17′24″	329 ± 25	$\alpha_{168}^{1400} \leq -1.52 \pm 0.04$	4.3	530
Abell 0133	P	×	01 ^h 02 ^m 40 ^s .8	−21°52′12″	-	-	-	-
	R or RG	×	-	-	-	-	-	-
Abell 0141	H	✓	01 ^h 05 ^m 33 ^s .6	−24°38′24″	110 ± 11	$\alpha_{168}^{610} \leq -2.1 \pm 0.1$	5.0	1100
Abell 2496	cR or cH	✓	22 ^h 50 ^m 52 ^s .8	−16°26′60″	561 ± 42	$\alpha_{74}^{1400} = -1.26 \pm 0.02$	~4.2	~560
Abell 2556	cP	✓	23 ^h 13 ^m 12 ^s .0	−21°28′12″	29.3 ± 5.5	$\alpha_{168}^{1400} = -1.22 \pm 0.14$	2.4	240
Abell 2680	cH	✓	23 ^h 56 ^m 31 ^s .2	−21°02′24″	23 ± 8	$\alpha_{168}^{1400} \leq -1.2 \pm 0.2$	~2.2	~400
Abell 2693	cH	✓	00 ^h 02 ^m 14 ^s .4	−19°33′00″	50 ± 6	$\alpha_{168}^{1400} \leq -0.88 \pm 0.06$	3.0	530
Abell 2721	cR or cH	✓	00 ^h 06 ^m 14 ^s .4	−34°43′48″	54 ± 14	$\alpha_{168}^{1400} \leq -0.96 \pm 0.12$	4.0	500
Abell 2744 ^e	H	×	00 ^h 14 ^m 19 ^s .2	−30°23′24″	550 ± 51	$\alpha_{168}^{1400} = -1.11 \pm 0.04$	~6.9	~1900
	R	×	00 ^h 14 ^m 38 ^s .4	−30°19′48″	237 ± 24	$\alpha_{168}^{1400} = -1.19 \pm 0.05$	~5.2	~1400
Abell 2751	R	✓	00 ^h 16 ^m 55 ^s .2	−31°23′24″	323 ± 62	$\alpha_{168}^{1400} = -1.27 \pm 0.11$	~8.7	~1000
APMCC 039	cR or RG	✓	00 ^h 17 ^m 50 ^s .4	−31°18′36″	60 ± 8	$-1.3(\pm 0.1) \leq \alpha_{168}^{1400} \leq -0.4(\pm 0.1)$	8.5	1000 ^f
Abell 2798	cR	✓	00 ^h 37 ^m 38 ^s .4	−28°30′36″	110 ± 9	$\alpha_{168}^{1400} = -1.2 \pm 0.1$	4.2	490
Abell 2811	cH or mH	✓	00 ^h 42 ^m 09 ^s .6	−28°31′48″	81 ± 17	$\alpha_{168}^{1400} \leq -1.5 \pm 0.1$	~3.4	~400
Abell 4038 ^c	P	×	23 ^h 47 ^m 40 ^s .8	−28°09′00″	4790 ± 250	-	-	-
Abell S0084	cH	✓	00 ^h 49 ^m 19 ^s .2	−29°30′36″	32 ± 5	$\alpha_{168}^{1400} \leq -1.3 \pm 0.1$	3.5	420
Abell S1099	U	✓	23 ^h 13 ^m 04 ^s .8	−23°08′24″	180 ± 20	$\alpha_{168}^{1400} = -1.0 \pm 0.2$	~9.5	~1100
Abell S1121	H or R	✓	23 ^h 25 ^m 14 ^s .4	−41°12′36″	80 ± 13	$\alpha_{168}^{843} = -1.2 \pm 0.2$	~3.6	~1100 ^g
Abell S1136	U	✓	23 ^h 36 ^m 19 ^s .2	−31°36′36″	586 ± 46	-	~6.8	~490
	cH	✓	23 ^h 51 ^m 02 ^s .4	−19°56′24″	87 ± 17	$\alpha_{168}^{1400} \leq -1.4 \pm 0.1$	~1.6	~370
RXC J2351.0–1954	cR (A)	✓	23 ^h 51 ^m 28 ^s .8	−19°59′24″	57 ± 9	$\alpha_{168}^{1400} \leq -1.2 \pm 0.1$	5.8	1400
	cR (B)	✓	23 ^h 50 ^m 21 ^s .6	−19°48′36″	147 ± 13	$\alpha_{168}^{1400} \leq -1.68 \pm 0.04$	5.4	1300
MACS J2243.3–0935 ^h	H	×	22 ^h 43 ^m 26 ^s .4	−09°35′24″	80 ± 40	$\alpha_{168}^{610} = -1.6 \pm 0.4$	-	-
GMBCG J357.91841–08.97978 ^j	cH	✓	23 ^h 51 ^m 38 ^s .4	−08°58′48″	128 ± 20	$\alpha_{168}^{1400} = -1.62 \pm 0.10$	3.2	1000
Abell S1063	H and RG ^k	✓	22 ^h 48 ^m 45 ^s .6	−44°30′36″	265 ± 38	$\alpha_{168}^{843} = -1.36 \pm 0.11$	-	-

^a Classification (H: radio halo; R: radio relic; P: radio phoenix; mH: mini-halo, RG: individual or blended [remnant] radio galaxy; U: undecided—requires further information; c: candidate object).

^b Flux-weighted average right ascension and declination of the emission, or peak flux density position if using aegean, or estimated central coordinates based on morphology.

^c Reported by Slee & Reynolds (1984).

^d Assuming a redshift of $z = 0.2395$.

^e Reported by Govoni et al. (2001).

^f Assuming a redshift of $z = 0.107$.

^g Assuming a redshift of $z = 0.3580$.

^h Reported by Cantwell et al. (2016).

^j We consider GMBCG J357.91841–08.97978 and WHL J235151.0-0.085929 to be the same cluster.

^k The emission is comprised of blended radio sources in data presented here, but Xie et al. (2020) report a radio halo.

^l Size deconvolved from the 2.3 arcmin beam.

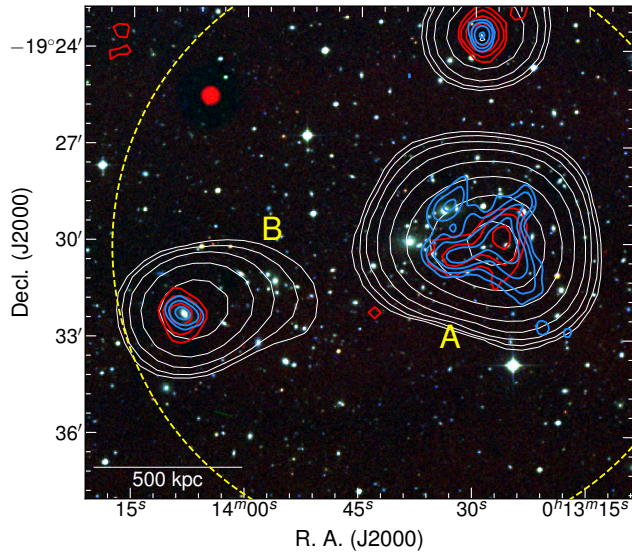


Figure 2. Abell 0013. DSS2 RGB image with contours overlaid as follows: EoR0 field, white, starting at 7 mJy beam^{-1} ; NVSS, red, beginning at $1.5 \text{ mJy beam}^{-1}$; TGSS, blue, beginning at $13.2 \text{ mJy beam}^{-1}$, all increasing with factors of 2. ‘A’ marks the relic. The dashed circle has a 1 Mpc radius centered on the cluster, and the linear scale is set at the cluster’s redshift.

3.2. Individual galaxy clusters

3.2.1. Abell 0013

Slee & Reynolds (1984) report the detection of a steep-spectrum radio phoenix in Abell 0013 at GHz frequencies with filamentary structure (see also Slee et al., 2001; George et al., 2017). We detect the same emission, shown as contours in Fig. 2 (labelled ‘A’), also detected in the NVSS and TGSS surveys. We measure $S_{168} = 1.85 \pm 0.13 \text{ Jy}$ with an LAS of 5.9 arcmin and largest linear scale (LLS) at the cluster’s redshift of 610 kpc. From the NVSS image we measure $S_{1400} = 28.7 \pm 4.1 \text{ mJy}$, resulting in a spectral index between 168–1400 MHz of $\alpha_{168}^{1400} = -1.96 \pm 0.08$. While classified as a radio phoenix, the SED is well-modelled by a power law in the frequency range here (George et al., 2017), though we note that the two-point index here is steeper than that reported by George et al. (2017) largely due to the NVSS measurement. We also note the detection of additional diffuse emission in the optical subcluster to the East of the phoenix, labelled ‘B’, connected to the nearby point source, though we cannot comment on its nature.

3.2.2. Abell 0022

Abell 0022 features extremely diffuse, faint emission that appears to permeate the cluster. Fig. 3 shows the emission extending from the centre of the cluster northward. We see from the NVSS and TGSS data that the MWA emission is coincident with three point sources: NVSS J002042–254239, associated with a member of the intervening galaxy triple DUKST 473–042; NVSS J002048–254437; and NVSS J002058–253957, emission associated with the clus-

ter member 2MASX J00205811–2539516. The MWA data extends considerably further north reminiscent of the cluster halo in Abell 3888 (Shakouri et al., 2016), though also appears connected to a steep-spectrum source that appears point-like at the MWA resolution to the East. We do not obtain a flux density measurement for the extended emission due to complex blending of sources.

XMM-Newton data is shown in the right panel of Fig. 3 (Obs. ID 0201900301, PI Böhringer), which were taken and reduced as part of the REXCESS survey (Böhringer et al., 2007; Pratt et al., 2009). The 168 MHz radio emission extends far beyond the X-ray emission, however some of the emission may coincide with the discrete point sources at the cluster center. We cannot unambiguously classify this emission but suggest a higher-resolution follow-up may reveal its nature.

3.2.3. Abell 0033

Fig. 4 shows emission on the periphery of both Abell 0033 ($z = 0.28$, photometric; Leir & van den Bergh 1977) and WHL J002712.5-193045 ($z = 0.2395$, spectroscopic; Wen & Han 2013). The white circles in Fig. 4 have 1 Mpc radii about the cluster centres. The two clusters are separated by an angular distance of ~ 80 arcsec, and given the clear concentration of optical galaxies seen in the DSS2 images, they are likely the same cluster and we hereafter consider there to be only Abell 0033 at the redshift of $z = 0.2395$. The grey, dashed contour in Fig. 4 is at the $2\sigma_{\text{rms}}$ level to indicate the possibility of the two objects, Obj. A and B, being a single piece of extended emission on the cluster periphery. If this is the case, the entire structure has a flux density of $S_{168} = 26 \pm 5 \text{ mJy}$, and an LAS is 6.3 arcmin which translates to an LLS of 1.4 Mpc at $z = 0.2395$. The NVSS does not show emission within the area of the 168 MHz emission. We provide an upper limit on the 1.4 GHz flux density of $S_{1400} \leq 10 \text{ mJy}$ resulting in $\alpha_{168}^{1400} \leq -0.4 (\pm 0.1)$, consistent with many radio sources and does not aid in classification. Potential optical IDs are highlight on Fig. 4, though neither provide further clarification on the classification of the source. While the source shares properties with radio relics and dead radio galaxies, we recommend sensitive follow-up observations of the source to confirm its nature.

3.2.4. Abell 0085

Slee & Reynolds (1984) report the detection of a phoenix offset from the centre of Abell 0085, and Giovannini & Feretti (2000) provide follow-up 300 MHz imaging with the VLA and ascertain an LLS for the source of 386 kpc (corrected for this cosmology). 168 MHz emission coincides with the previously detected phoenix (Obj. A in Fig. 5), with $S_{168} = 9.39 \pm 0.96 \text{ Jy}$. The TGSS shows 147.5 MHz emission beyond that of the NVSS despite similar resolutions with an extended structure to the southeast, tracing the emission at 300 MHz shown by Giovannini & Feretti. From the MWA, TGSS, and 300-MHz data we find $\alpha_{147.5}^{300} = -1.85 \pm 0.03$, though note that the TGSS image is likely missing flux due to resolution and missing short baselines, which suggests

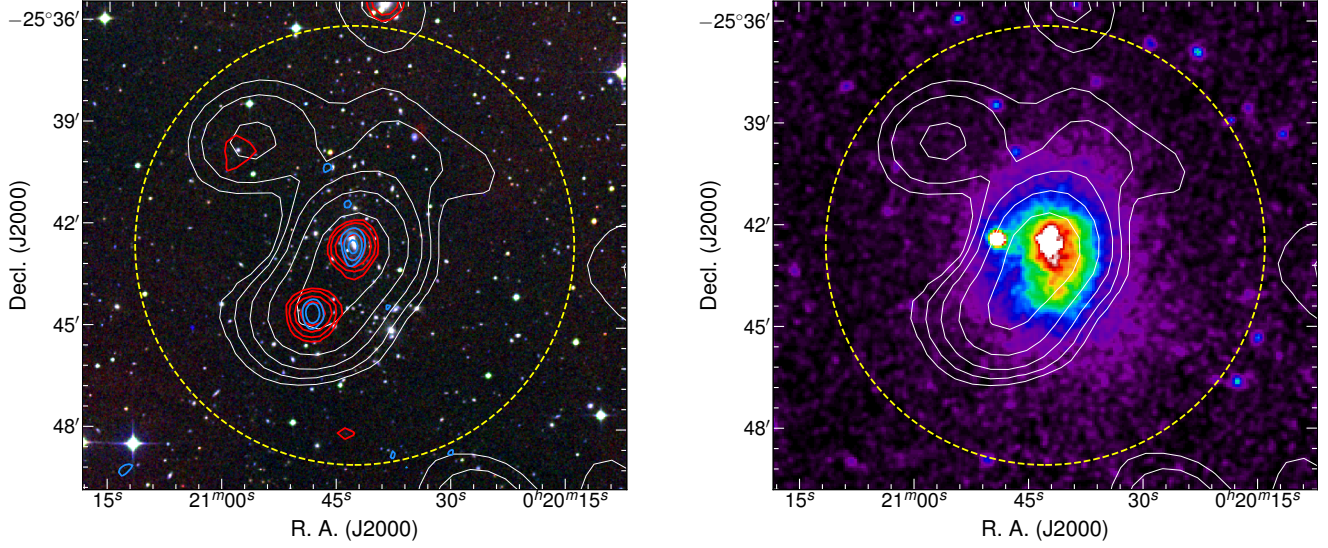


Figure 3. Diffuse emission within Abell 0022. *Left:* DSS2 RGB image with contours overlaid as follows: EoR0 field, white, beginning at 7 mJy beam^{-1} ; NVSS, red, beginning at $1.5 \text{ mJy beam}^{-1}$; TGSS, blue, beginning at 21 mJy beam^{-1} . Image features as in Fig. 2. *Right:* Exposure corrected, smoothed XMM-Newton image from the REXCESS survey with EoR0 contours overlaid as in the left panel.

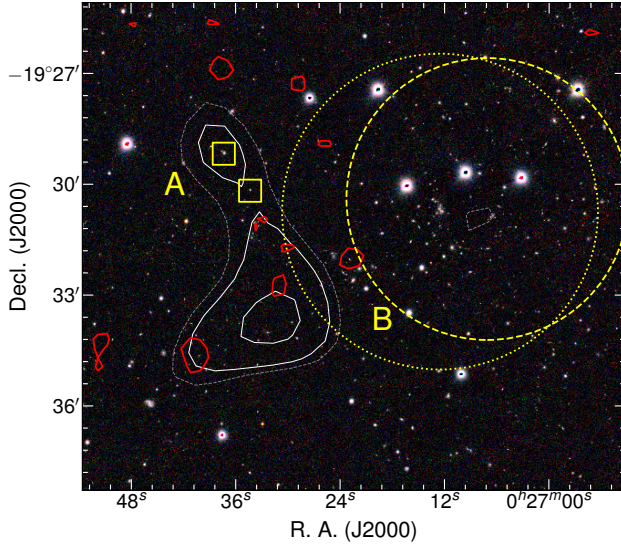


Figure 4. Candidate relic on the periphery of Abell 0033. The background is a PS1 RGB image with contours overlaid as follows: EoR0, white, $3\sigma_{\text{rms}}$ beginning at $6.9 \text{ mJy beam}^{-1}$ and a single grey, dashed, $2\sigma_{\text{rms}}$ contour at $4.6 \text{ mJy beam}^{-1}$; NVSS, red, beginning at $1.5 \text{ mJy beam}^{-1}$. No TGSS emission is seen above the $3\sigma_{\text{rms}}$ level of $25.8 \text{ mJy beam}^{-1}$. The dashed circle is centre on the position of Abell 0033 and the dotted circled is centred on WHL J002712.5-193045, both with 1 Mpc radii at the reported redshifts. They are suspected to be the same cluster (see main text). The boxes indicate possible optical IDs for the diffuse emission.

the relic may have an even steeper spectral index. Given the small frequency range and the SED shown by Slee et al. (2001), we suggest a power law in this regime adequately models the observed data. We measure an LAS of 6.7 arcmin (LLS of 430 kpc). The radio source to the southeast of the relic (Obj. B in Fig. 5) has extended 168 MHz emis-

sion beyond the source seen in the NVSS which is likely associated with the galaxy SDSS J004150.17-092547.4. The TGSS 147.5 MHz data shows two distinct sources within this extended, steep-spectrum emission. The right panel of Fig. 5 shows a zoomed-in view of Obj. B, with EoR0 field contours overlaid on exposure corrected, smoothed XMM-Newton data (Obs. ID 0723802201, PI de Plaa). Obj. B features an extension to the bulk of the X-ray emitting plasma at the cluster's core. Kempner et al. (2002) suggest that this extension of X-ray emission, along with the complex of radio sources Obj. B, is representative of subcluster asymmetrically merging with the main cluster of Abell 0085.

3.2.5. Abell 0122

Abell 0122 features a strong extended source at its centre with a flux density of $S_{168} = 329 \pm 25 \text{ mJy}$ and LAS of 4.3 arcmin (with an LLS of 530 kpc). There is no significant 1.4 GHz emission seen with the NVSS image, though the 147.5 MHz TGSS data shows extended emission morphologically similar to a head-tail radio galaxy. We provide a 1.4 GHz flux limit of $S_{1400} \leq 13 \text{ mJy}$ and a corresponding spectral index of $\alpha_{168}^{1400} \leq -1.52 \pm 0.04$.

The right panel of Fig. 6 shows exposure corrected, smoothed XMM-Newton data (Obs ID 0504160101, PI Sivanandam). The 168 MHz radio emission fills the X-ray plasma. Abell 0122 shows no evidence in the either X-ray emission or the optical density that would suggest the cluster is undergoing, or had undergone, a merger event and the source size points towards towards a mini-halo if not a radio galaxy, though we cannot confirm the classification here.

3.2.6. Abell 0133

Abell 0133 has been studied extensively in X-ray (e.g. Re-

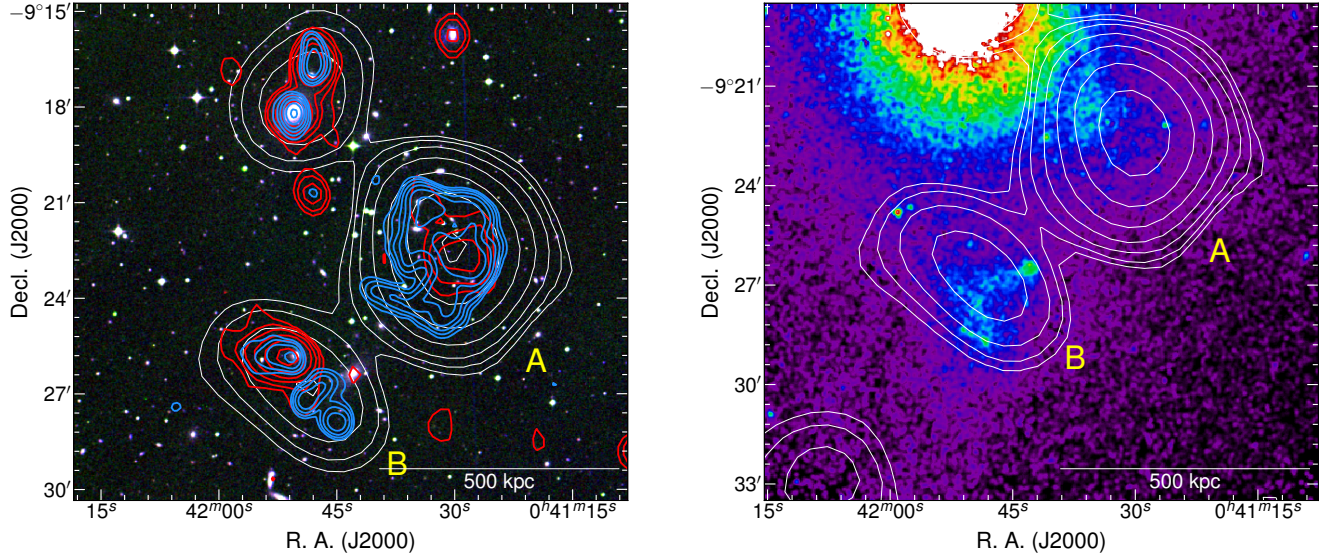


Figure 5. Abell 0085. *Left:* DSS2 RGB image with contours overlaid as follows: EoR0 field, white, beginning at $49.7 \text{ mJy beam}^{-1}$; NVSS, red, beginning at $1.5 \text{ mJy beam}^{-1}$; TGSS, blue, beginning at $9.6 \text{ mJy beam}^{-1}$. *Right:* Exposure corrected, smoothed XMM-Newton image with EoR0 contours overlaid as in the left panel. Note that the right panel has a smaller field of view and is centred to show the subcluster ‘A’. Both panels show the linear scale at the cluster’s redshift.

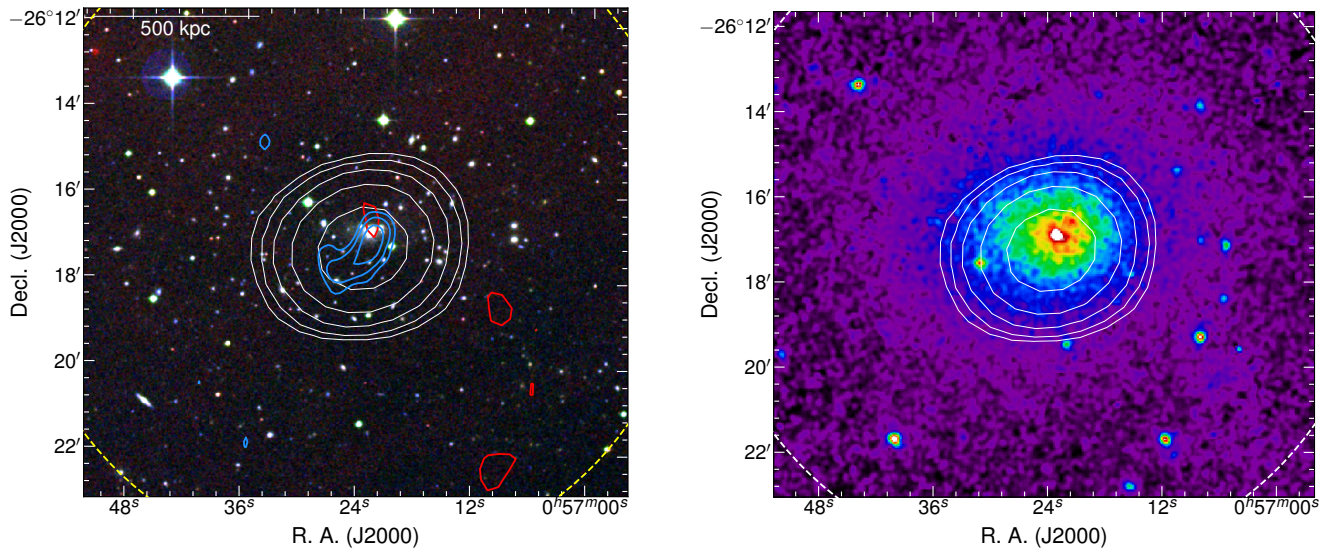


Figure 6. Steep-spectrum emission at the centre of Abell 0122. *Left:* DSS2 RGB image with contours overlaid as follows: EoR0 field, white, beginning at 12 mJy beam^{-1} ; NVSS, red, beginning at $1.5 \text{ mJy beam}^{-1}$; TGSS, blue, beginning at $13.5 \text{ mJy beam}^{-1}$. The linear scale is at the cluster’s redshift. *Right:* Exposure corrected, smoothed XMM-Newton image with EoR0 field contours overlaid as in the left panel.

ichert et al., 1981; Fujita et al., 2002, 2004) along with the multi-wavelength study by Randall et al. (2010) which all point towards the disturbed, dynamic nature of the cluster. A radio phoenix was detected by Slee & Reynolds (1984, but see also Slee et al. 2001). A weak shock coincides with the phoenix source (Fujita et al., 2004).

Fig. 7 shows the cluster centre with the emission of interest, with Obj. A a large, possible lobe, Obj. B the radio phoenix, and the orange square indicating the possible ID for double-lobe-like structure, along with Obj. C, an interesting knot-like feature. Randall et al. (2010) discuss the possibility that the

entire structure is a giant, background radio galaxy. As part of this interpretation, the phoenix is thought to be a separate entity. We consider an alternative explanation not covered by Randall et al. (2010) where the southern lobe ‘A’ is a radio relic. This explanation is akin to the relic in 1E 0657-56 (the Bullet Cluster; Liang et al., 2000, 2001; Shimwell et al., 2014, 2015; Srinivasan, 2015). Liang et al. (2000) show low resolution radio imaging of the Bullet Cluster, and further X-ray observations provide high resolution imaging to show the directionality of the shock (Markevitch, 2006) with clear diffuse emission located to the east of the west-ward

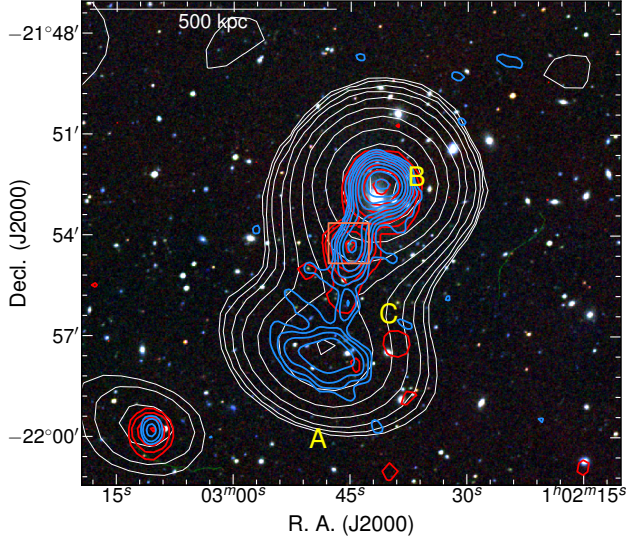


Figure 7. The centre of Abell 0133. DSS2 RGB image with contours overlaid as follows: EoR0 field, white, beginning at 15 mJy beam^{-1} ; NVSS, red, beginning at $1.5 \text{ mJy beam}^{-1}$; TGSS, blue, $13.2 \text{ mJy beam}^{-1}$. The linear scale is at the redshift of the cluster, and Obj. A, ‘B’, and ‘C’ are discussed in the text.

X-ray shock. This piece of diffuse emission is considered a relic, created through back-shock of the massive, merging system (Shimwell et al., 2014). We consider the possibility of a similar relic in Obj. A. Figure 6 of Randall et al. (2010) shows *Chandra* data overlaid with 1400 and 330 MHz radio data, indicating the potential relic sitting beyond the X-ray emission towards the periphery of the cluster. Obj. C in Fig. 7 marks a knot in the filament, clear in the blue TGSS contours, and seen in Figure 5(d) of Randall et al. (2010). This has no optical ID so is not necessarily an unassociated point source. The structure (‘A’–‘C’–part of ‘B’) is considered to be a GRG (Randall et al., 2010). The supposed optical host (at ‘C’) has a redshift of $z = 0.2930$ (2MASX J01024529-2154137; Owen et al., 1995; Slee et al., 2001; Randall et al., 2010) placing it far behind Abell 0133. We find that the 147.5 MHz TGSS contours in Fig. 7 show that the peak of this emission near the core of the GRG does not align with the proposed optical ID, marked with an orange square, though the 1.4 GHz NVSS contours do align well with 2MASX J01024529–2154137.

If the emission is that of a radio galaxy, we find LAS to be 10.1 arcmin, which at $z = 0.2930$ corresponds to an LLS of 2.7 Mpc and at $z = 0.0562$ an LLS of 660 kpc. In the relic scenario, we measure east-west dimensions: the LAS is found to be 5.5 arcmin (an LLS of 360 kpc at the cluster’s redshift). We cannot confirm the nature of the emission with the available data. In Table 5 we list the phoenix, as well as the ambiguous emission as either a radio galaxy or radio relic.

3.2.7. Abell 0141

We present a hitherto undetected radio halo at the centre of Abell 0141 coinciding with the optical concentration of

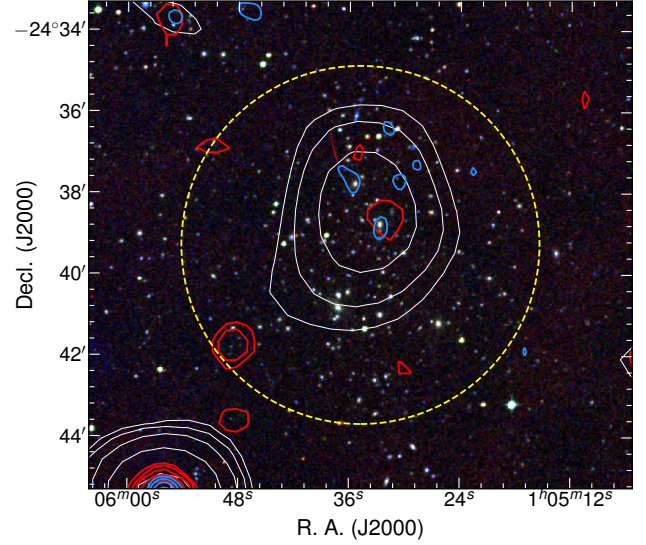


Figure 8. Radio halo at the centre of Abell 0141. DSS2 RGB image with contours overlaid as follows: EoR0 field, white, beginning at 10 mJy beam^{-1} ; NVSS, red, beginning at $1.5 \text{ mJy beam}^{-1}$; TGSS, blue, beginning at $13.8 \text{ mJy beam}^{-1}$. The dashed circle is centred on the cluster with a 1 Mpc radius.

galaxies. The left panel of Fig. 8 shows the cluster with an RGB image as a background with the EoR0 field contours overlaid to illustrate the radio halo’s location relative to the cluster. Previously, Venturi et al. (2007, 2008) reported a non-detection at 610 MHz with the GMRT with an upper limit of $S_{610} \leq 7.0 \text{ mJy}$, assuming a standard spectral index of -1.3 . From the EoR0 field image, the radio halo is measured to have a flux density of $S_{168} = 110 \pm 11 \text{ mJy}$ and an LAS of 5.0 arcmin (LLS of 1.1 Mpc). This suggests a spectral index of $\alpha_{168}^{610} \leq -2.1 \pm 0.1$. This places the halo within Abell 0141 at least equal in spectral steepness to the halo detected in Abell 0521, which has an average spectral index of $\alpha \approx -2.1$ (Brunetti et al., 2008).

Çaglar (2018) have performed an X-ray analysis of the cluster, suggesting it may be in an early stage of the merger with both the northern and southern subclusters being described as “moderately disturbed non-cool core structures”. Additionally, Dahle et al. (2002) comment on the ill-defined optical centre, noting that the two optical density peaks occur ~ 2 arcmin apart, consistent with the X-ray emission. Radio halos have been found in pre-merging clusters (Abell 0399 and Abell 0400; Murgia et al., 2010, and in MACS J0416.1-2403; Ogrean et al. 2015), and in these known cases it is likely that each of the subclusters hosts its own halo. This may be the case here, where the source we detect is the convolution of a radio halo in each of the northern and southern subclusters. Future work with the Australian Square Kilometre Array Pathfinder (ASKAP) will provide insight into the nature of this radio halo (Duchesne et al., in prep.).

3.2.8. Abell 2496

Fig. 9 shows the centre of Abell 2496 with extended, dif-

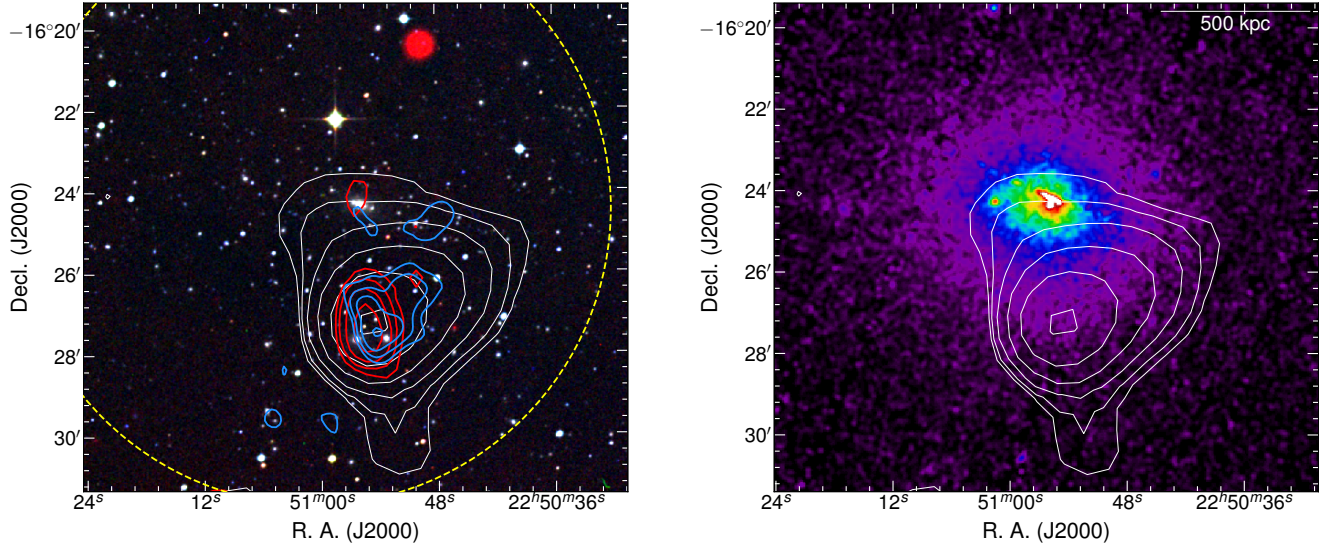


Figure 9. Diffuse emission within Abell 2496. *Left:* DSS2 RGB image with contours overlaid as follows: EoR0 field, white, beginning at 15 mJy beam^{-1} ; NVSS, red, beginning at $1.5 \text{ mJy beam}^{-1}$. TGSS, blue, 12 mJy beam^{-1} . *Right:* Exposure corrected, smoothed XMM-Newton data with EoR0 field contours overlaid as in the left panel. The dashed circle is centred on the MCXC coordinates with radius of 1 Mpc.

fuse emission with an irregular morphology. We measure $S_{168} = 561 \pm 42 \text{ mJy}$ within the full EoR0 field contours, and obtain $S_{1400} = 37.7 \pm 2.0 \text{ mJy}$ (Condon et al., 1998), $S_{147.5} = 659.4 \pm 67.0 \text{ mJy}$ (Intema et al., 2017), and $S_{74} = 1340 \pm 250 \text{ mJy}$ (Lane et al., 2014). From these measurement we obtain $\alpha_{74}^{1400} = -1.26 \pm 0.02$. We note that the NVSS and TGSS contours may represent a discrete cluster source, with the extended components in the EoR0 field and TGSS data separate emission such as a radio halo. Additionally, the TGSS data may be resolving out some of the emission if the full EoR0 field contours comprise a single source.

The bulk of the radio emission is offset from the X-ray emission seen with the exposure corrected, smoothed XMM-Newton data in the right panel of Fig. 9 (Obs. ID 0765030801, PI Reiprich). The radio emission does extend towards the X-ray peak. If the total radio emission represents a single source, we measure an LAS of $\sim 4.2 \text{ arcmin}$ (LLS of $\sim 560 \text{ kpc}$). In this case, this may be a “face-on” radio relic. If the NVSS contours represent a discrete cluster source, then extended lower frequency emission may represent a mini-halo, however, we cannot confirm the nature of the source with the present data.

3.2.9. Abell 2556 and Abell 2554

Fig. 10 shows the two clusters Abell 2556 and Abell 2554 which have centres within 13 arcmin of each other, but have redshifts of $z = 0.0871$ and $z = 0.1108$ (Caretta et al., 2002) respectively. To the north of Abell 2556, 1 Mpc from its centre (east of Abell 2554, over 1 Mpc) an elongated diffuse source is seen, labelled ‘A’ in Fig. 10, with flux densities $S_{168} = 29.3 \pm 5.5 \text{ mJy}$ and $S_{1400} = 2.2 \pm 0.5 \text{ mJy}$ (Condon et al., 1998), corresponding to $\alpha_{168}^{1400} = -1.22 \pm 0.14$. The LAS of the source is 2.4 arcmin (LLS of 240 kpc at $z =$

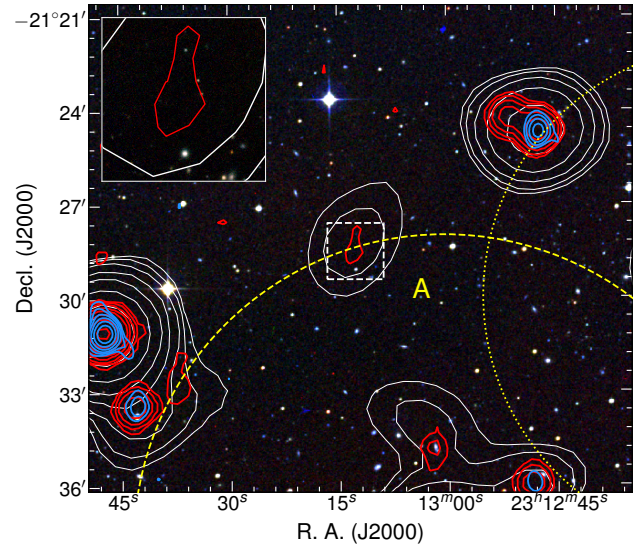


Figure 10. Diffuse emission, Obj. A, in Abell 2556. DSS2 RGB image with contours overlaid as follows: EoR0 field, white, beginning at 10 mJy beam^{-1} ; NVSS, red, beginning at $1.5 \text{ mJy beam}^{-1}$; TGSS, blue, beginning at $13.4 \text{ mJy beam}^{-1}$. The dashed circle is centred on Abell 2556 and the dotted circle on Abell 2554, each with radii of 1 Mpc. The inset is the PS1 data with its location indicated on the image as a dashed, white box. EoR0 field and NVSS contours are shown on the inset as in the main figure.

0.0871). No optical host is seen in the PS1 inset in Fig. 10 at the centre of the emission. Too small for a radio relic, we note that radio phoenixes are more often found towards cluster centres but this would be consistent with the spectral index, where phoenixes closer to the centre become much steeper. We consider this a candidate radio phoenix.

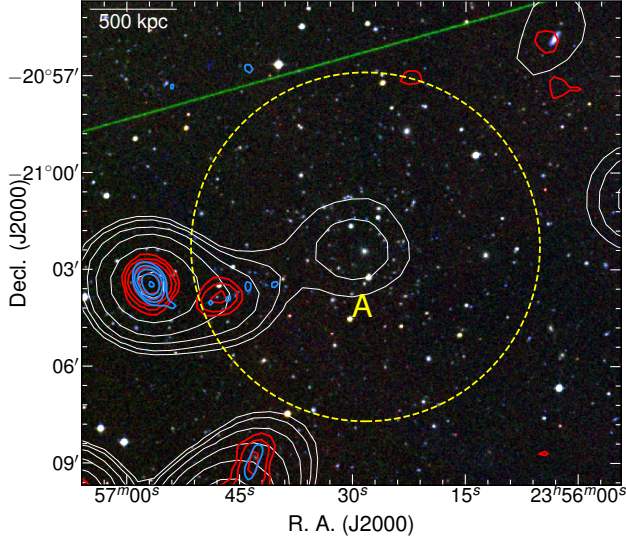


Figure 11. Abell 2680 with a candidate halo marked with an ‘A’. DSS2 RGB image with contours overlaid as follows: EoR0 field, white, beginning at 7 mJy beam^{-1} ; NVSS, red, beginning at $1.5 \text{ mJy beam}^{-1}$; TGSS, blue, beginning at $11.1 \text{ mJy beam}^{-1}$. The dashed circle has a 1 Mpc radius about the cluster centre.

3.2.10. Abell 2680

Fig. 11 shows a patch of steep-spectrum emission at the centre of Abell 2680, with no counterparts in the NVSS or TGSS images (Obj. A). The emission may be slightly elongated east-west, though this apparent elongation may just be the result of blending with the eastern sources. We make an approximate measurement of the flux density yielding $S_{168} = 22.8 \pm 8.0 \text{ mJy}$, where the uncertainty is given by Eq. 1 with an additional contribution to account for the slight blending to the east. We estimate a 1.4 GHz upper limit of 1.8 mJy giving $\alpha_{168}^{1400} \leq -1.2 \pm 0.2$. The LAS is estimated to be $\sim 2.2 \text{ arcmin}$ (LLS of $\sim 400 \text{ kpc}$). The physical extent of the source and coincidence with the cluster centre core suggests a cluster halo. This particular case requires observations at different resolutions to determine if the source is actually extended but we consider this a candidate radio halo or mini-halo.

3.2.11. Abell 2693

Abell 2693 is found to host an extended source at its centre. We consider this a candidate halo, marked ‘A’ in Fig. 12, has an LAS of 3.0 arcmin (LLS of 530 kpc). We measure $S_{168} = 50 \pm 6 \text{ mJy}$ and $S_{1400} \leq 7.7 \text{ mJy}$ from the NVSS image, resulting in $\alpha_{168}^{1400} \leq -0.88 \pm 0.06$. The spectral index limit is inconclusive in the halo classification, however, the location and size suggest that it may be a halo, and we classify this emission as a candidate halo.

To the west of the cluster there is an elongated steep-spectrum source marked B in Fig. 12, though it appears as a point source in the TGSS image.

3.2.12. Abell 2721

Fig. 13 shows Abell 2721. Diffuse radio emission is seen at

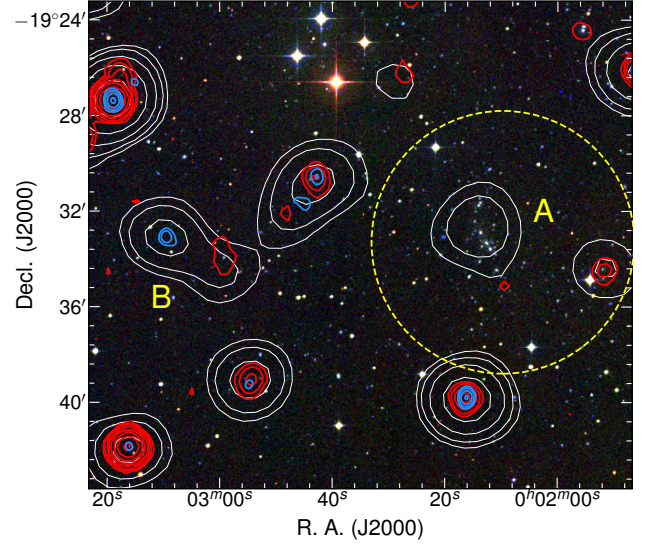


Figure 12. Candidate radio halo A and steep-spectrum source B within and nearby Abell 2693. DSS2 RGB image with contours overlaid as follows: EoR0 field, white, beginning at 10 mJy beam^{-1} ; NVSS, red, beginning at $1.5 \text{ mJy beam}^{-1}$; TGSS, blue, beginning at 12 mJy beam^{-1} . The dashed circle is centred on the cluster and has a 1 Mpc radius.

168 MHz offset to the east of the cluster centre (Obj. A). The lack of emission seen in the NVSS or SUMSS suggests a steep spectral index, and a lack of emission in TGSS is likely due to lack of sensitivity. We estimate LAS of the emission to be $\sim 4.0 \text{ arcmin}$ (LLS of $\sim 500 \text{ kpc}$).

As part of the ATCA REXCESS Diffuse Emission Survey (ARDES), deep 1.4 and 2.1 GHz imaging of the cluster was obtained with the ATCA, finding no evidence of a halo (Shakouri et al., 2016). An upper limit to the emission is $S_{1400} \leq 7 \text{ mJy}$ (Shakouri, private comms.). After subtraction of the blended point sources, we find $S_{168} = 54 \pm 14 \text{ mJy}$ for the extended emission, resulting in $\alpha_{168}^{1400} \leq -0.96 \pm 0.12$.

The right panel of Fig. 13 shows the REXCESS X-ray data overlaid with MWA contours. The extended radio emission is offset from the X-ray peak, ruling out a halo. A relic-type source is possible, but the spectral index likely rules out a phoenix. We suggest this source may be a relic viewed somewhat along the line of sight, and consider it a candidate radio relic.

3.2.13. Abell 2744

Abell 2744 is a *Hubble* Frontier Fields cluster (Lotz et al., 2017) showing gravitational lensing of the high-redshift background galaxies (see e.g. Castellano et al., 2016). Fig. 14 shows Abell 2744 with both a centrally located giant radio halo (GRH, defined to have an LLS $> 1 \text{ Mpc}$) and a megaparsec scale radio relic on its northeast periphery (Govoni et al., 2001). Both of these objects are seen in the EoR0 field at 168 MHz, blending together along the northeast edge of the cluster. The GRH fills the entire cluster out to 1 Mpc having an approximate LLS of 1.9 Mpc (LAS of $\sim 6.9 \text{ arcmin}$) and the relic with an LLS on the order 1.4 Mpc (LAS

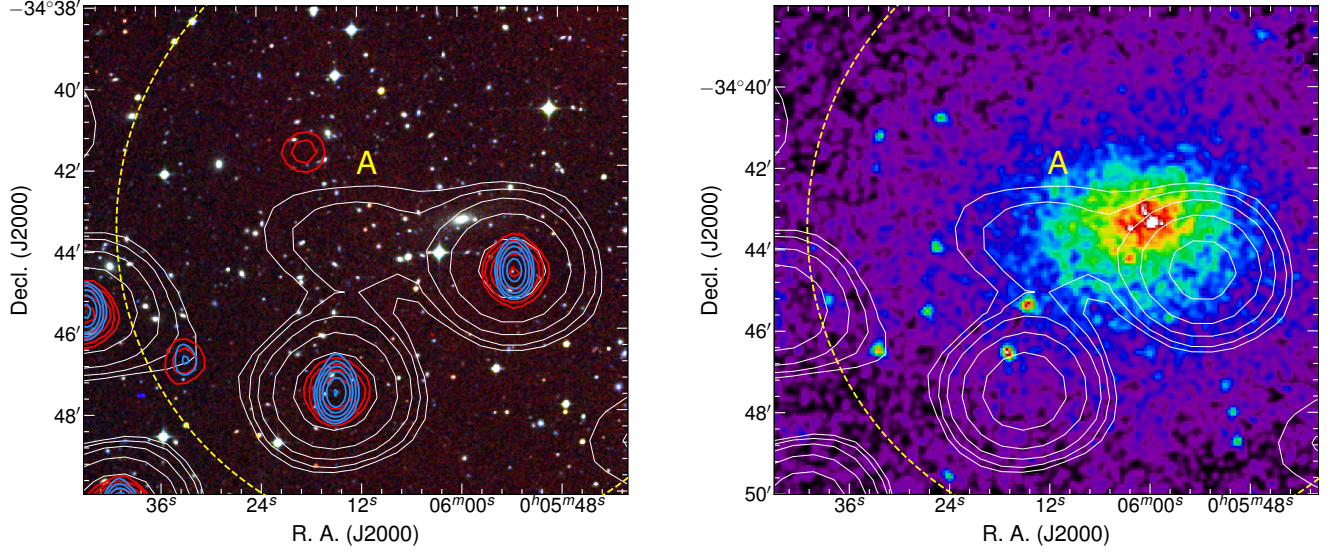


Figure 13. Diffuse emission within Abell 2721, marked with an ‘A’. *Left:* DSS2 RGB image with contours overlaid as follows: EoR0 field, white, beginning at 10 mJy beam^{-1} ; NVSS, red, beginning at $1.5 \text{ mJy beam}^{-1}$; TGSS, blue, beginning at $8.1 \text{ mJy beam}^{-1}$. *Right:* Exposure corrected, smoothed XMM-Newton X-ray image from the REXCESS survey with EoR0 contours overlaid as in the left panel. The dashed circle is centred on the cluster with a radius of 1 Mpc.

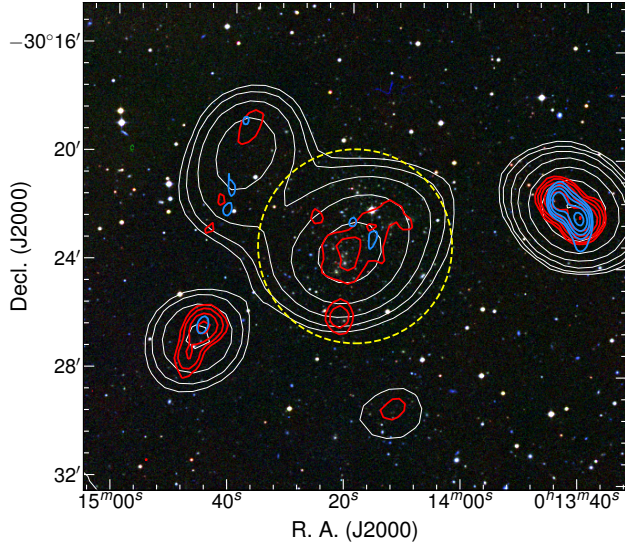


Figure 14. Abell 2744 with giant radio halo and relic. DSS2 RGB image with contours overlaid as follows: EoR0 field, white, beginning at 10 mJy beam^{-1} ; NVSS, red, beginning at $1.5 \text{ mJy beam}^{-1}$; TGSS, blue, beginning at $12.9 \text{ mJy beam}^{-1}$. The dashed circle is centred on the cluster with a radius of 1 Mpc.

~ 5.2 arcmin).

With *aegean*, with fit Gaussians to the relic and GRH to decompose and measure the emission, finding $S_{168}^{\text{halo}} = 550 \pm 51 \text{ mJy}$ and $S_{168}^{\text{relic}} = 237 \pm 24 \text{ mJy}$. From these and literature measurements (Venturi et al., 2013) we find $\alpha_{\text{halo}} = -1.11 \pm 0.04$ and $\alpha_{\text{relic}} = -1.19 \pm 0.05$, consistent with spectral indices reported by Venturi et al. (2013).

3.2.14. Abell 2751 and APMCC 039

Abell 2751 and APMCC 039 have an angular separation of 17.7 arcmin and redshifts of $z = 0.107$ (Struble & Rood, 1999) and $z = 0.082$ (Dalton et al., 1997), respectively. Fig. 15 shows the two clusters, with the dashed and dotted circles indicating 1 Mpc radii about the cluster centres at their reported redshifts. The small yellow squares indicate galaxies with redshifts in the range 0.1–0.114, which is $cz \approx 2000 \text{ km s}^{-1}$ around the redshift of Abell 2751. There are no galaxies in the vicinity at the reported redshift of APMCC 039. From this galaxy distribution we suggest the clusters are likely interacting or are otherwise a single system.

We detect a new candidate relic to the east of Abell 2751 (Obj. A in Fig. 15), blending with the point source NVSS J001648–312223. The 168 MHz emission appears to simply be a radio tail extending from NVSS J001648–312223, however the 147.5 MHz TGSS emission is resolved enough to show that the emission is not necessarily associated with the point source. After subtraction of the flux density contribution of the blended point source, $S_{168}^{\text{relic}} = 323 \pm 62 \text{ mJy}$. We consider this emission a candidate radio relic. We also measure $S_{1400}^{\text{relic}} = 22 \pm 3 \text{ mJy}$ from the NVSS map and obtain $\alpha_{168}^{1400} = -1.27 \pm 0.11$, consistent with relic sources. We measure the LAS to be ~ 8.7 arcmin (LLS of ~ 1.0 Mpc).

Obj. B north of APMCC 039 also may be a relic or HT radio galaxy. We measure $S_{168} = 60 \pm 8 \text{ mJy}$ and an LAS of 8.5 arcmin (LLS of 1.0 Mpc at $z = 0.107$). With a limit from the NVSS we obtain $-1.3(\pm 0.1) \leq \alpha_{168}^{1400} \leq -0.4(\pm 0.1)$ consistent with either scenario. While this may be a relic, we suggest the likeliest case is a HT radio galaxy.

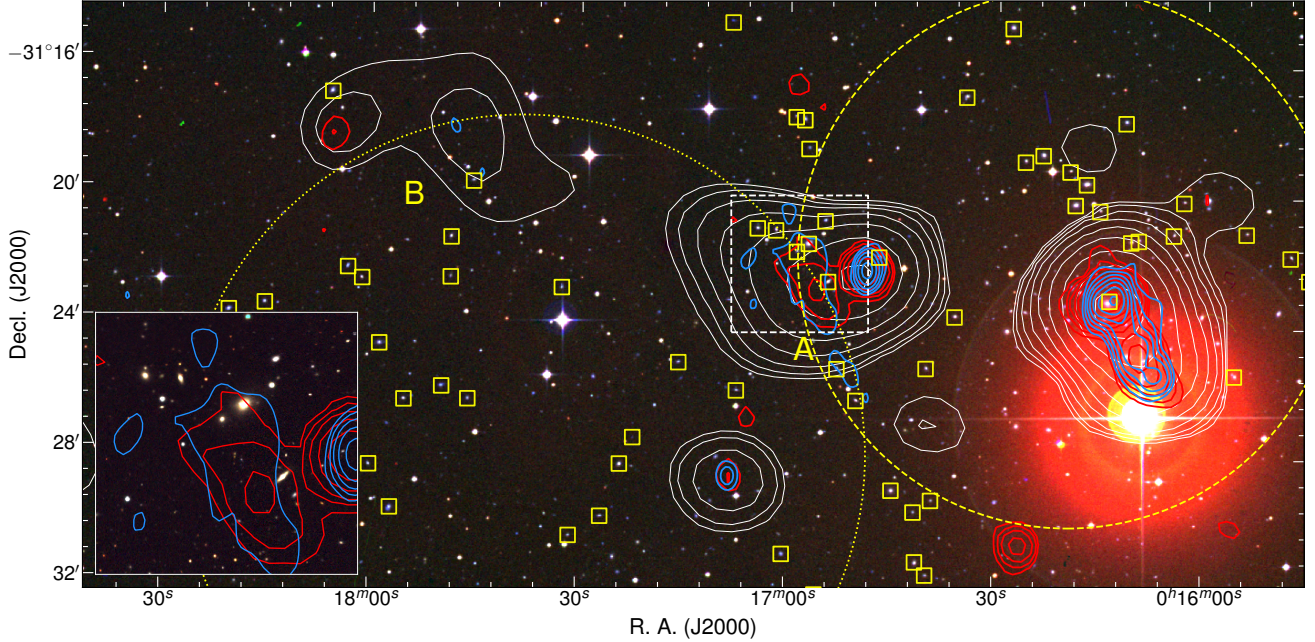


Figure 15. A candidate relic and a faint radio galaxy, near Abell 2751 and APMCC 039, marked as A and B. DSS2 RGB image with contours overlaid as follows: EoR0 field, white, beginning at 7 mJy beam^{-1} ; NVSS, red, beginning at $1.5 \text{ mJy beam}^{-1}$; TGSS, blue, beginning at $13.5 \text{ mJy beam}^{-1}$. The dashed circle is centred on Abell 2751 and the dotted on APMCC 039, each with radii of 1 Mpc. The squares indicate galaxies with redshifts in the range $0.1 \leq z \leq 0.114$. The inset of Obj. A is the DES DR1 data with its location indicated by the dashed, white box. TGSS and NVSS contours are overlaid as in the main image.

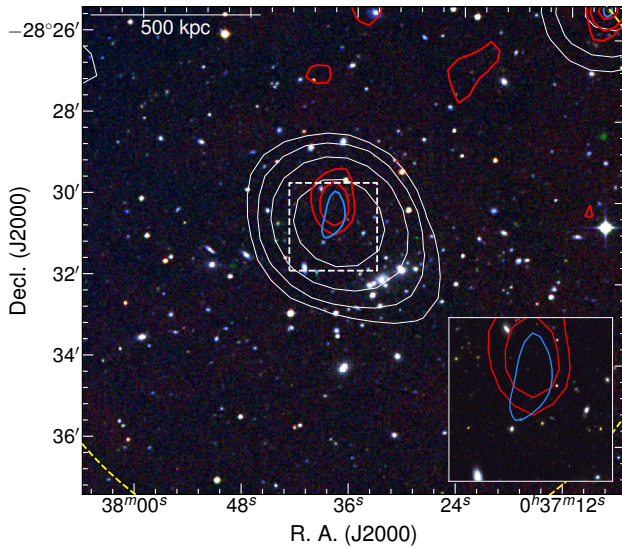


Figure 16. Candidate radio relic within Abell 2798. DSS2 RGB image with contours overlaid as follows: EoR0 field, white, beginning at 7 mJy beam^{-1} ; NVSS, red, beginning at $1.5 \text{ mJy beam}^{-1}$; TGSS, blue, beginning at $13.8 \text{ mJy beam}^{-1}$. The inset is the DES DR1 data with its location indicated by the dashed, white box. NVSS contours are overlaid as in the main image.

3.2.15. Abell 2798

Fig. 16 shows the centre of Abell 2798 hosting a steep-spectrum radio source, slightly offset from centre. We find $S_{168} = 110 \pm 9 \text{ mJy}$ and an LAS of 4.2 arcmin (an LLS of

490 kpc). Both the TGSS and NVSS surveys show extended emission offset slightly from the centroid of the 168 MHz emission. There are no obvious optical IDs for this emission. The NVSS source is NVSS J003738–283008 and has a flux density of $S_{1400} = 9.0 \pm 1.3 \text{ mJy}$ (Condon et al., 1998). This yields a spectral index for the source of $\alpha_{168}^{1400} = -1.2 \pm 0.1$. The RASS broad band (0.1–2.4 keV) count image shows no significant X-ray emission within the cluster which is consistent with the low cluster mass. We classify this emission similarly to that in Abell 0013: a candidate radio phoenix either near the cluster centre or projected onto it. Further high-resolution imaging will be necessary to fully determine the nature of this emission.

3.2.16. Abell 2811

The left panel of Fig. 17 shows Abell 2811. At the centre of the cluster we make a new detection of a faint radio halo (Obj. A). As part of the XMM-Newton survey of the soft X-ray background Henley & Shelton (2013) consider this emission a galactic halo, however, Sivanandam et al. (2009) note that the surrounding X-ray emission is offset from the BCG by 27 arcsec ($\sim 55 \text{ kpc}$), which suggests that the cluster is in a dynamic, merging state and that the 168 MHz radio emission seen in Fig. 17 is a cluster halo. The XMM-Newton data (Obs. ID 0404520101, PI Sivanandam) shown in Fig. 17 reveals slight N-S elongation of the ICM, further hinting at the dynamical state.

This radio halo is on the order of $\sim 3.4 \text{ arcmin}$ (LLS of $\sim 400 \text{ kpc}$). Measuring $S_{168} = 81 \pm 17 \text{ mJy}$ and $S_{1400} <$

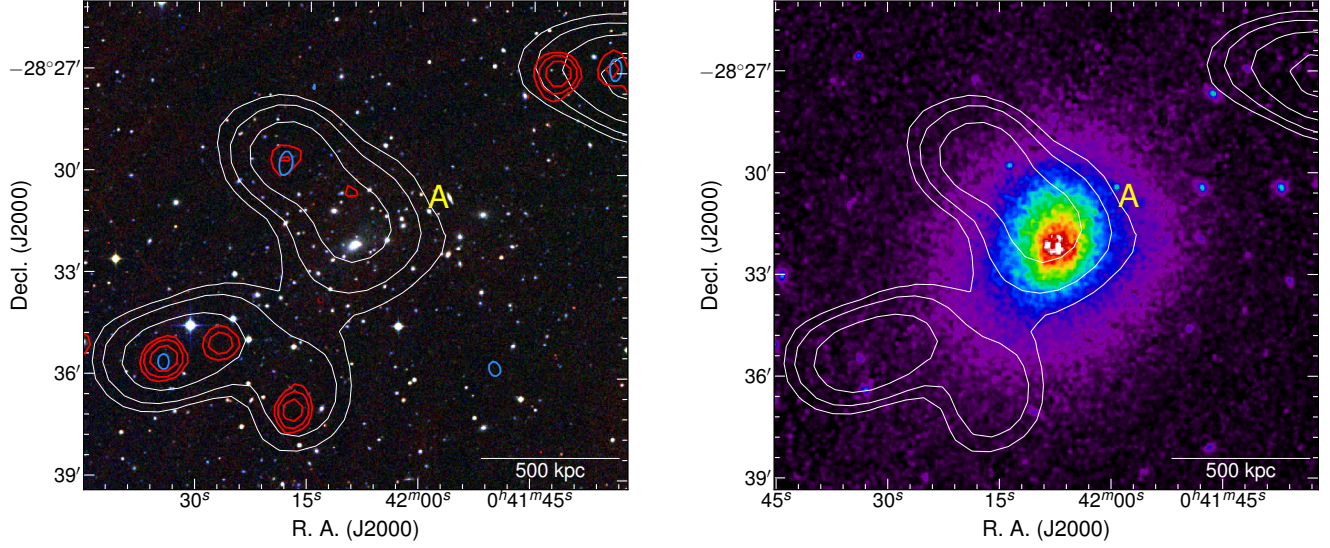


Figure 17. Radio halo within Abell 2811, marked with an ‘A’. *Left*: DSS2 RGB image with contours overlaid as follows: EoR0 field, white, beginning at 7 mJy beam^{-1} ; NVSS, red, beginning at $1.5 \text{ mJy beam}^{-1}$; TGSS, blue, beginning at $12.6 \text{ mJy beam}^{-1}$. *Right*: Exposure corrected, smoothed XMM-Newton X-ray image of Abell 2811 with the EoR0 field contours overlaid as in the left panel. In both panels the linear scale is at the redshift of the cluster.

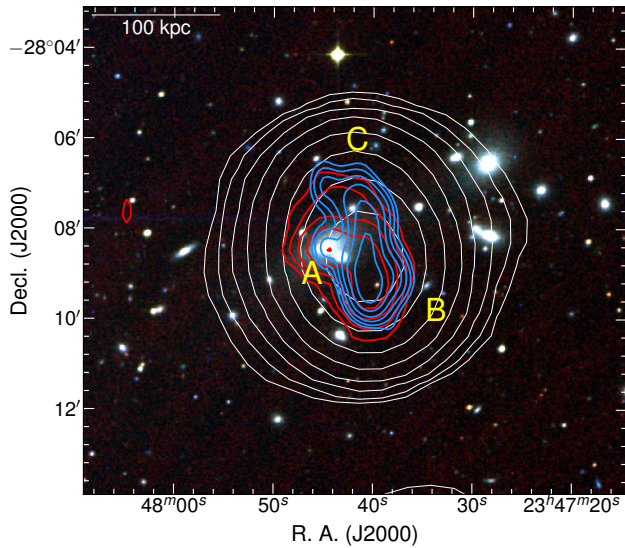


Figure 18. The centre of Abell 4038. DSS2 RGB image with contours overlaid as follows: EoR0 field, white, beginning at 20 mJy beam^{-1} ; NVSS, red, beginning at $1.5 \text{ mJy beam}^{-1}$; TGSS, blue, beginning at 20 mJy beam^{-1} . Marked objects are described in the text.

3.1 mJy we find $\alpha_{168}^{1400} \leq -1.5 \pm 0.1$. This would class this as an ultra-steep spectrum radio halo (USSRH; e.g. Cassano et al., 2006; Brunetti et al., 2008).

3.2.17. Abell 4038

Slee & Reynolds (1984) report a steep-spectrum source (Obj. B and C in Fig. 18), and Slee & Roy (1998); Slee et al. (2001) follow-up and class it as a radio phoenix. The emission of the phoenix blends with the radio emission from IC 5358 and 2MASX J23474209–2807335 (Obj. A in Fig. 18). From

measurements provided by Kale & Dwarakanath (2012); Slee et al. (2001); Finlay & Jones (1973) we subtract flux density contributions from discrete cluster sources and measure $S_{168} = 4.79 \pm 0.25 \text{ Jy}$ for the phoenix.

3.2.18. Abell S0084

We detect diffuse radio emission at the centre of Abell S0084 (Fig. 19). The cluster was part of the ARDES sample of Shakouri et al. (2016) though no diffuse emission was detected at the centre of the cluster. We measure $S_{168} = 32 \pm 5 \text{ mJy}$ and calculate a limit of $S_{1400} \leq 2.2 \text{ mJy}$ from the rms noise in the ARDES data (Shakouri, priv. comms.). This results in $\alpha_{168}^{1400} \leq -1.3 \pm 0.1$. We measure an LAS of 3.5 arcmin (LLS of 420 kpc).

The right panel of Fig. 19 shows the REXCESS X-ray data with MWA contours overlaid. There is no cavity present in the X-ray data to suggest that the emission could be the lobes of an AGN and thus may be associated with the cluster itself. Further, Abell S0084 is not a cool core cluster (Pratt et al., 2009) and so we do not suspect this emission is a mini-halo. Given that the radio emission sits offset from the X-ray peak by $\sim 100 \text{ kpc}$ and that the X-ray plasma appears undisturbed, we only tentatively classify this as a candidate radio halo, though note that the emission may be from a centrally located radio galaxy, possibly dying or otherwise of old age.

3.2.19. Abell S1099

Fig. 20 shows Abell S1099 as an RGB image with MWA, NVSS, and TGSS contours overlaid. The cluster hosts extended, diffuse emission coincident with one of the BCGs, 2MASX J23130574-2308369 ($z = 0.1086 \pm 0.0002$; Caretta et al. 2004), which coincides with the peak of the emission at 168 MHz . We measure an LAS of $\sim 9.5 \text{ arcmin}$ (LLS

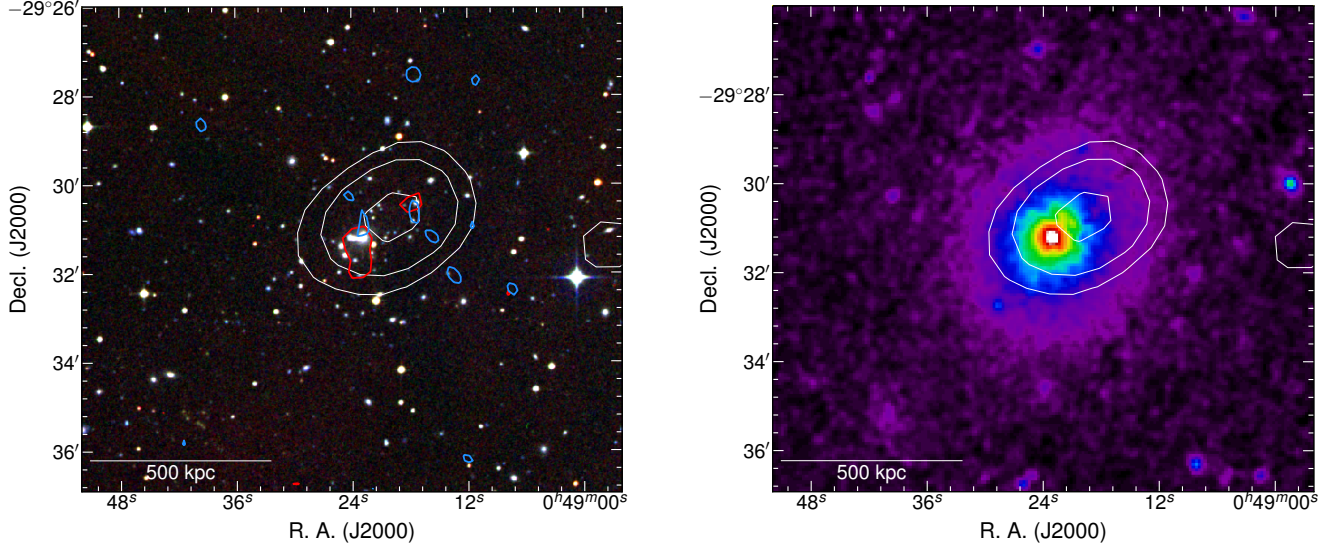


Figure 19. The centre of Abell S0084. *Left:* DSS2 RGB image with contours overlaid as follows: EoR0 field, white, beginning at 7 mJy beam^{-1} ; NVSS, red, beginning at $1.5 \text{ mJy beam}^{-1}$; TGSS, blue, beginning at 12 mJy beam^{-1} . *Right:* Exposure corrected, smoothed XMM-Newton X-ray image from the REXCESS survey with EoR0 contours overlaid as in the left panel along with X-ray contours.

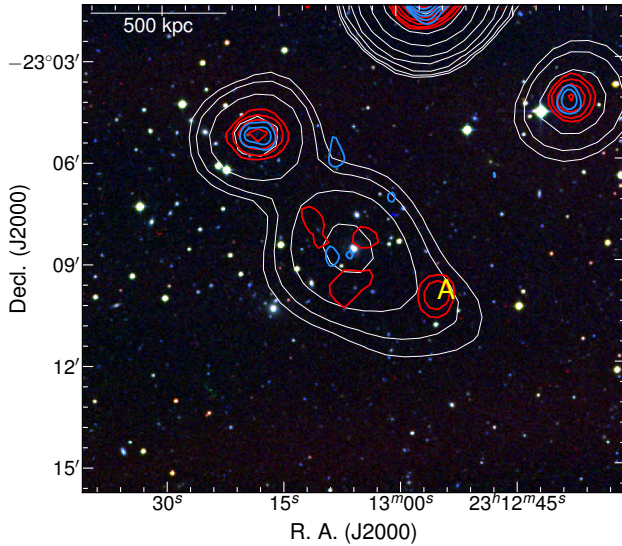


Figure 20. Diffuse emission in Abell S1099. DSS2 RGB image with contours overlaid as follows: EoR0 field, white, beginning at 10 mJy beam^{-1} ; NVSS, red, beginning at $1.5 \text{ mJy beam}^{-1}$; TGSS, blue, beginning at $11.1 \text{ mJy beam}^{-1}$. The linear scale is at the redshift of Abell S1099. ‘A’ marks a likely embedded source.

of $\sim 1.1 \text{ Mpc}$). We measure $S_{168} = 180 \pm 20 \text{ mJy}$, where the uncertainty includes a term to account for the slight blending towards the northwestern source. Further, Obj. A in Fig 20 appears to be an embedded point source, catalogued as NVSS J231255–230959 (Condon et al., 1998), which is not accounted for. We convolve the NVSS image to $108.87 \text{ arcsec} \times 108.87 \text{ arcsec}$ and obtain $S_{1400} = 22.3 \pm 6.4 \text{ mJy}$. This yields $\alpha_{168}^{1400} = -1.0 \pm 0.2$. This is consistent with radio halos or perhaps an intervening radio relic. Without significant X-ray emission detected by *ROSAT*, we suggest it is

unlikely to be a radio halo. We cannot confirm the nature of the emission presently.

3.2.20. Abell S1121

We detect diffuse emission in Abell S1121 located near the cluster centre, with counterpart emission in SUMSS (Fig. 21). Note the artefacts in the SUMSS data from a nearby bright source (top left contour in Fig. 21). Abell S1121 is reported by Coziol et al. (2009) to have a redshift of $z = 0.19043$ though Liu et al. (2015) report a redshift of $z = 0.3580$ for this system. The left panel of Fig. 21 shows galaxies with available redshifts in the range $cz \approx 2000 \text{ km s}^{-1}$ around the reported redshifts, with the small circles associated with $z = 0.19043$ and the small boxes associated with $z = 0.3580$. Given the location and numbers of each galaxy distribution, we consider the emission (and the cluster) to be at the redshift reported by Liu et al. (2015), $z = 0.3580$. There is likely a separate, intervening system along the line-of-sight that Coziol et al. (2009) are measuring.

The right panel of Fig. 21 shows archival *Chandra* data (Obs. ID 13405, PI Garmire, exposure time 8.94 ks, 0.1–13.1 keV). This X-ray emitting plasma is situated in the core of the cluster, but shows cone-like morphology suggesting a complex dynamical state. A significant component of the low-frequency emission coincides with the X-ray emission. We measure the flux density within an approximate region around the source, obtaining $S_{168} = 80 \pm 13 \text{ mJy}$. The SUMSS emission does not coincide with the radial artefacts so is real and we measure $S_{843} = 11 \pm 2 \text{ mJy}$ yielding $\alpha_{168}^{843} = -1.2 \pm 0.2$. We do not detect significant emission in the TGSS data suggesting no significant point source contribution.

We estimate an LAS of $\sim 3.6 \text{ arcmin}$ (LLS of $\sim 1.1 \text{ Mpc}$ at $z = 0.3580$). The slight offset from the X-ray centroid and the

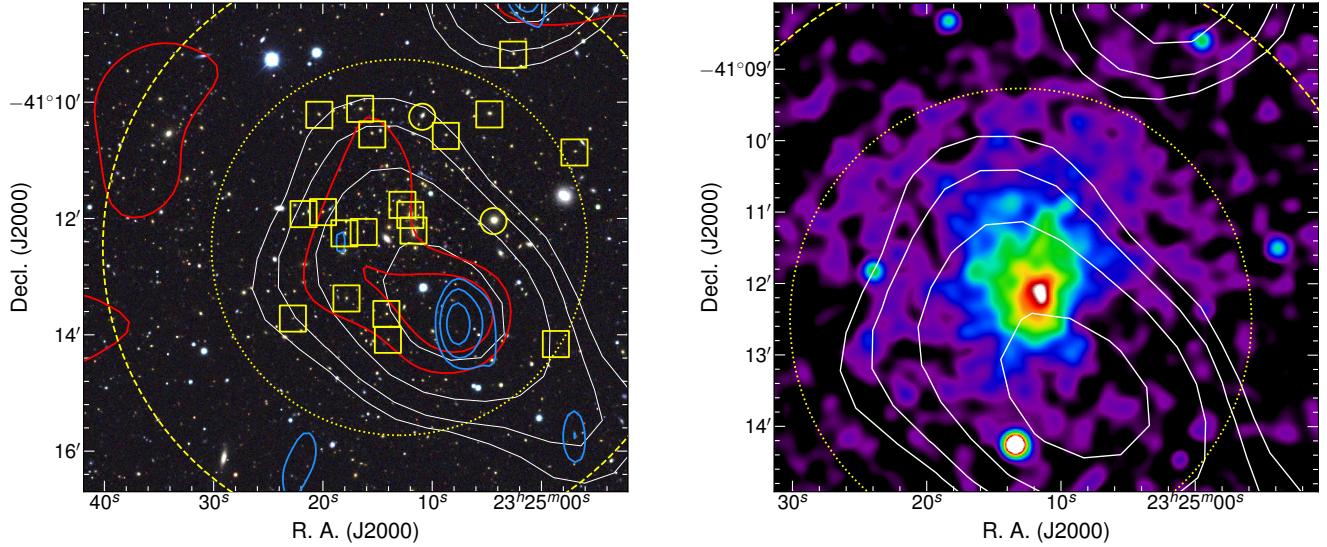


Figure 21. Candidate radio halo within Abell S1121. *Left:* DES DR1 RGB image with contours overlaid as follows: EoR0, 15 mJy beam⁻¹; smoothed SUMSS, red, beginning at 7 mJy beam⁻¹; and TGSS, purple, beginning at 13.8 mJy beam⁻¹. The dashed and dotted circles are centred on the cluster with 1 Mpc radii at each of the reported redshifts. The squares and small circles indicate galaxies with available redshifts within $cz \approx 2000$ km s⁻¹ at the two reported redshifts (see text). *Right:* Smoothed, archival *Chandra* data with EoR0 contours as in the left panel. Note that the right panel has a smaller field of view as the *Chandra* image does not cover the entire region shown in the left panel—the dotted and dashed circles are identical to those in the left panel.

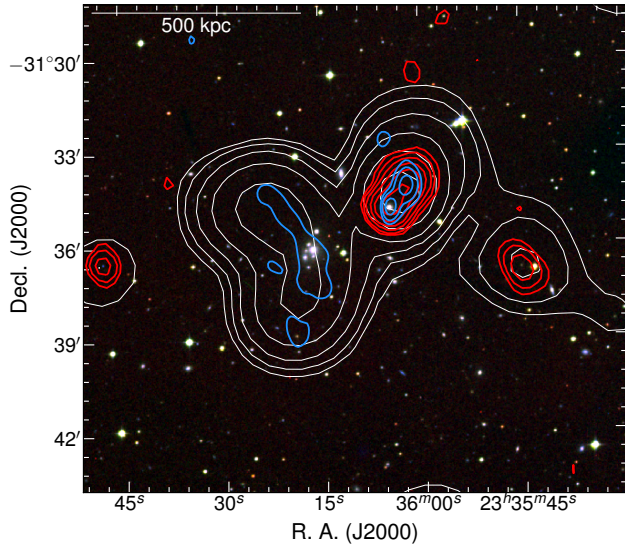


Figure 22. Diffuse emission within Abell S1136. DSS2 RGB image with contours overlaid as follows: EoR0 field, white, beginning at 10 mJy beam⁻¹; NVSS, red, beginning at 1.5 mJy beam⁻¹; TGSS, blue, beginning at 14.4 mJy beam⁻¹. The linear scale is at the cluster redshift.

elongation in SUMSS might suggest a radio relic, perhaps intervening along the line of sight, though the properties are consistent with a radio halo.

3.2.21. Abell S1136

Fig. 22 shows the centre of Abell S1136 with elongated diffuse radio emission appearing strongly at 168 MHz, with a

patchy counterpart in the TGSS survey at 147.5 MHz. There is no corresponding 1.4 GHz or 843 MHz emission seen in the NVSS or SUMSS surveys suggesting a steep spectrum. The total flux density of the diffuse source is decomposed using *aegean* and measured to be $S_{168} = 586 \pm 46$ mJy.

The RASS broad-band 0.1–2.4 keV image does not show particularly strong X-ray emission at the centre, and the RGB image (Fig. 22) shows the optical concentration of galaxies at the centre is offset towards the west of the bulk of the 168 MHz emission. The elongation is north-south, with an almost bent double-lobed structure, and has an LAS of ~ 6.8 arcmin (LLS of ~ 490 kpc). While the emission could be classified as a cluster halo, alternate explanations are those of cluster relic intervening along the line-of-sight towards the cluster, or a dead radio galaxy likely having a previous association with the BCG, ESO 470-G020. Without polarisation data and higher resolution imaging we do not classify this emission here. This cluster will be investigated further using ASKAP data (Macgregor et al., in prep.).

3.2.22. RXC J2351.0–1954

The left panel of Fig. 23 shows RXC J2351.0–1954 (PSZ1 G057.09–74.45) and the surrounding field, and the right panel shows the central region of the cluster. The dotted and dashed circles are centered on the RXC and PSZ1 coordinates, respectively. In the left panel of Fig. 23 two steep-spectrum, diffuse sources are located to the southeast (Obj. A) and northwest (Obj. B). The right panel shows extended emission coinciding with the optical center, marked as Obj. C. Chon & Böhringer (2012) report this cluster as X-ray luminous.

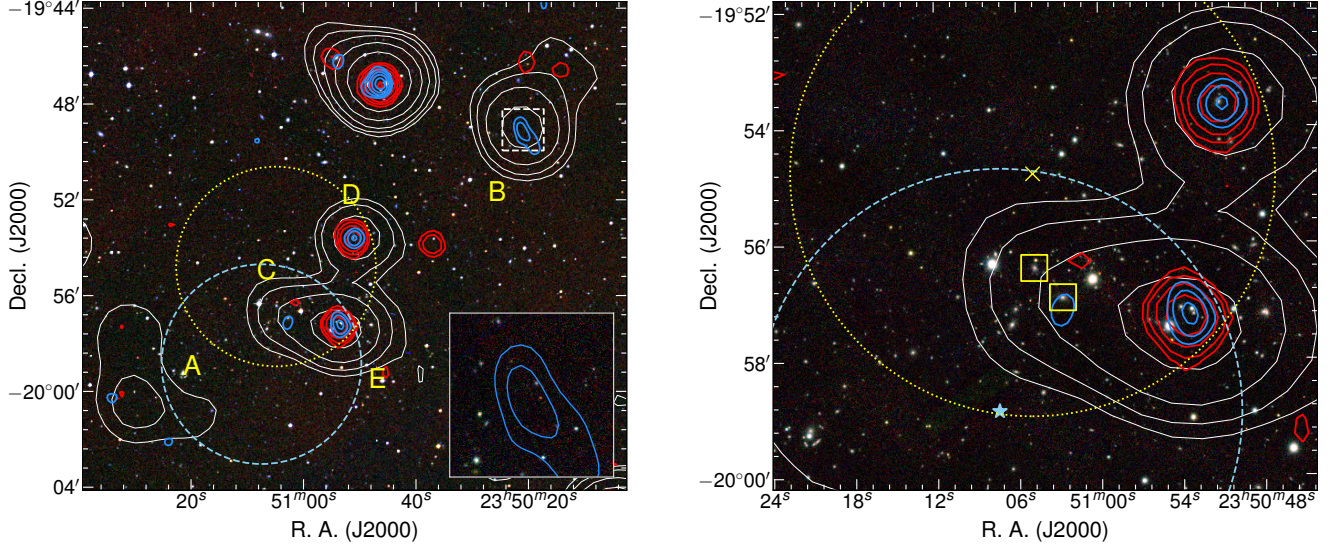


Figure 23. RXC J2351.0–1954. *Left:* DSS2 RGB image with contours overlaid as follows: EoR0 field, white, beginning at 10 mJy beam^{-1} ; NVSS, red, beginning at $1.5 \text{ mJy beam}^{-1}$; TGSS, blue, beginning at $13.8 \text{ mJy beam}^{-1}$. The dashed, blue circle is centred on the PSZ1 coordinates, and a dotted, yellow circle is centred on the X-ray coordinates, both with radii of 1 Mpc. ‘A’ and ‘B’ mark candidate relics, ‘C’ a candidate halo, and ‘D’ and ‘E’ are other radio sources mentioned in the text. The inset is the PS1 data with its location indicated on the image as a dashed, white box. The TGSS contours are shown on the inset as in the main figure. *Right:* A smaller field of view of the left panel with PS1 RGB background, a cross to denote the cluster’s coordinates given by Chon & Böhringer (2012), a star to denote the coordinates given by PSZ1, and squares showing galaxies with spectroscopic redshifts in the region.

Obj. A (left panel Fig. 23) may be a radio relic, with no optical ID and no counterpart emission in either NVSS or SUMSS. We measure $S_{168}^A = 57 \pm 9 \text{ mJy}$ and $S_{1400}^A \leq 4.2$, yielding $\alpha_{168}^{1400,A} \leq -1.2 \pm 0.1$, consistent with relic sources. A has an LAS of 5.8 arcmin (LLS of 1.4 Mpc). We consider Obj. A a candidate relic.

Obj. B (left panel Fig. 23 and inset) is a candidate for a second relic on the opposite side of the cluster to Obj. A. B is significantly brighter than A, with partial detection in the TGSS data but no detection at 1.4-GHz with the NVSS. There is no visible optical ID. We measure $S_{168}^B = 147 \pm 13 \text{ mJy}$ and $S_{1400}^B \leq 4.7 \text{ mJy}$, yielding $\alpha_{168}^{1400,B} \leq -1.68 \pm 0.04$. We measure an LAS of 5.4 arcmin (LLS of 1.3 Mpc) and it is located 2.8 Mpc away from the cluster center—an extreme distance for a radio relic (the largest relic distance is $\sim 3 \text{ Mpc}$, reported by Cuciti et al., 2018). We consider this a candidate radio relic.

Located near the cluster center, between the two reported centers, Obj. C may be a faint radio halo. We subtracted the flux density contributions of Obj. E and D (left panel of Fig. 23) from the total emission within contours of the Obj. C+D+E complex after extrapolation using NVSS and TGSS measurements. This results in $S_{168} = 87 \pm 17 \text{ mJy}$. We estimate a corresponding limit of $S_{1400} \leq 4.3 \text{ mJy}$ from the NVSS data, yielding $\alpha_{168}^{1400} \leq -1.4 \pm 0.1$, consistent with radio halo sources. We estimate an LAS of $\sim 1.6 \text{ arcmin}$ (LLS of $\sim 370 \text{ kpc}$), though note the source blending into Obj. E makes its full extent unclear. Without supplementary archival *Chandra* or *XMM-Newton* data (and note its reported center is based on *ROSAT* data) it is difficult to definitively classify

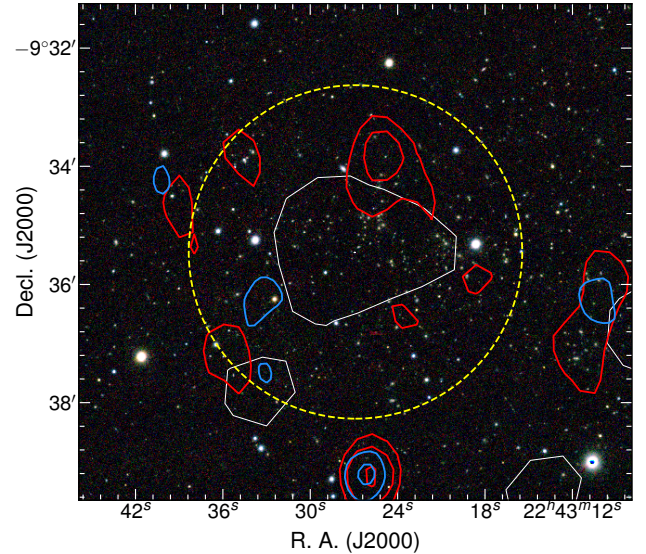


Figure 24. MACS J2243.3–0935 with radio halo. PS1 RGB image with contours overlaid as follows: EoR0 field, white, beginning at 60 mJy beam^{-1} ; NVSS, red, beginning at $1.5 \text{ mJy beam}^{-1}$; TGSS, blue, beginning at $10.2 \text{ mJy beam}^{-1}$. The dashed circle is centred on the cluster with a radius of 1 Mpc.

this emission. Nevertheless, given the location between the reported X-ray and SZ centres, we consider this a newly detected candidate radio halo.

3.2.23. MACS J2243.3–0935

Cantwell et al. (2016) report the detection of a ra-

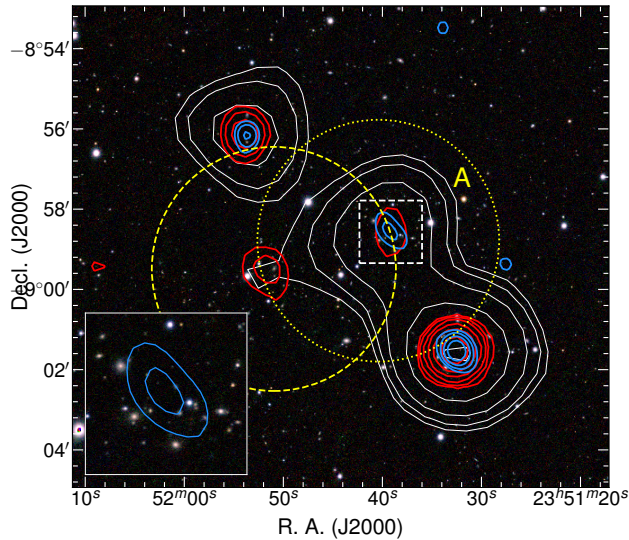


Figure 25. Diffuse emission on the periphery of WHL J235151.0–085929 or centre of GMBCG J357.91841–08.97978. PS1 RGB image with contours overlaid as follows: EoR0 field, white, beginning at 10 mJy beam^{-1} ; NVSS, red, beginning at $1.5 \text{ mJy beam}^{-1}$; TGSS, blue, beginning at $11.7 \text{ mJy beam}^{-1}$. The dashed circle is centred on the PSZ1 coordinates of WHL J235151.0–085929 with radius 1 Mpc. The dotted circle is centred on the cluster GMBCG J357.91841–08.97978 with the same 1 Mpc radius. The inset is the PS1 data with its location indicated on the image as a dashed, white box. The TGSS contours are shown on the inset as in the main figure.

dio halo in the merging cluster MACS J2243.3–0935 (MCXC J2243.3–0935; PSZ1 G056.94–55.06), detected using the Karoo Array Telescope-7 telescope and GMRT. Fig. 24 shows the MWA contours overlaid on the RGB image. MACS J2243.3–0935 is near the edge of the EoR0 field where the rms noise is highest. Because of this, the detection is tentative. Fig. 24 shows the cluster with $2\sigma_{\text{rms}}$ contours to emphasise this. At this level we measure the 168 MHz flux density to be $S_{168} = 80 \pm 40 \text{ mJy}$. With the 610 MHz flux density measured by Cantwell et al. (2016) we obtain a spectral index of $\alpha_{168}^{610} = -1.6 \pm 0.4$. These results should be taken with caution due to the noise in this region of the EoR0 field. In particular, the source size is not sufficient to be considered extended and without the previous detection at 610 and 1826 MHz by Cantwell et al. (2016) of the halo we would not consider this detection sufficient to consider the emission as real and extended.

3.2.24. GMBCG J357.91841–08.97978 and WHL J235151.0–085929

Fig. 25 shows the cluster WHL J235151.0–085929 (PSZ1 G082.31–67.01, dashed circle) with an RGB background and radio contours overlaid. Obj. A is a possible diffuse source on the cluster’s periphery. The cluster does not show significant X-ray emission in the RASS broad-band image. The location of the emission relative to the cluster centre and the lack of optical ID (see the inset on Fig. 25) are sug-

gestive of a cluster relic. Similarly, the NVSS and TGSS data show slightly extended emission, though the 1.4-GHz NVSS detection is at reasonably low significance. We measure an LAS of 3.2 arcmin (LLS of 1.0 Mpc). The NVSS catalogue flux density is $S_{1400} = 4.1 \pm 0.6 \text{ mJy}$ (Condon et al., 1998). With *aegean* with find $S_{168} = 128 \pm 20 \text{ mJy}$, resulting in $\alpha_{168}^{1400} = -1.62 \pm 0.10$.

We note that the Gaussian Mixture Brightest Cluster Galaxy (GMBCG; Hao et al., 2010) catalogue reports a cluster at the centre of the emission: GMBCG J357.91841–08.97978, with a photometric redshift of $z = 0.4$, and the emission may reside within this cluster. If this is the case the steep spectral index and central location would imply a cluster halo. The two clusters, WHL J235151.0–085929 and GMBCG J357.91841–08.97978, have centres separated by ~ 2.7 arcmin which at $z = 0.3939$ is $\sim 890 \text{ kpc}$. This separation in both angular distance and redshift would suggest either the clusters may be interacting or that they are the same cluster. With this in mind we suggest that the emission is a candidate cluster halo, at a redshift of $z = 0.3939$, associated with the cluster GMBCG J357.91841–08.97978.

3.2.25. Abell S1063

Abell S1063 is a *Hubble* Frontier Fields cluster and features heavy gravitational lensing of the distant optical galaxies (see e.g. Diego et al., 2016). The cluster is near the Southern edge of the EoR0 field and so is more affected by noise. Despite this, above a 50 mJy beam^{-1} level, a diffuse and elongated piece of emission is seen within the cluster. Exposure corrected, smoothed XMM-*Newton* data (Obs. ID 0504630101, PI Andersson) shows strong X-ray emission coinciding with the 168 MHz radio emission though their respective peaks lie offset from one another, with the X-ray peak situated at the position of the BCG (see Fig. 26). The X-ray emission can be seen to extend further northeast with the peak of the 168 MHz emission occurring in this same direction. The BCG, LCRS B224549.3-444744, with redshift $z = 0.34711 \pm 0.00025$ (Guzzo et al., 2009) is marked with a square in Fig. 26.

While the EoR0 field 168-MHz data may suggest a radio halo, the higher-resolution ATCA data at 2-GHz reveals the emission to be made up of four individual discrete sources (seen as contours in the left panel of Fig. 26), including the BCG. We find that the BCG has $\alpha_{1332}^{2868} = -1.05 \pm 0.03$, and the apparent spectral steepness of the emission is likely due to contribution from this source.

Despite the discrete sources in the cluster, during the preparation of this paper⁹ Xie et al. (2020) reported the detection of a radio halo from 325–3000 MHz, though the data presented here are unable to provide a clear detection.

4. Discussion

⁹During the three year hiatus since the original submission.

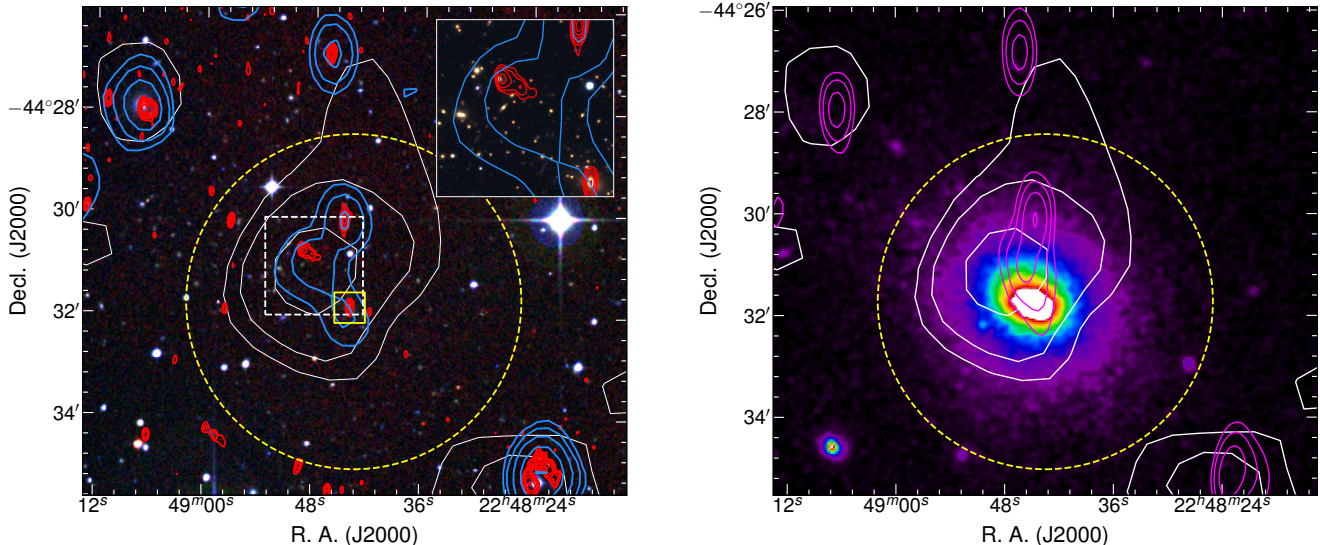


Figure 26. Abell S1063. *Left:* DSS2 RGB image with contours overlaid as follows: EoR0 field, white, beginning at 50 mJy beam^{-1} ; ATCA-stacked, red, beginning at $72 \mu\text{Jy beam}^{-1}$; ATCA-tapered, blue, beginning at $1.08 \text{ mJy beam}^{-1}$. The small box indicates the BCG of the cluster. The inset is the DES DR1 data with its location indicated by the dashed, white box. ATCA contours are overlaid as in the main image. *Right:* Exposure corrected, smoothed XMM-Newton image with contours EoR0 field contours overlaid as in the left panel, but with TGSS contours, magenta, beginning at $7.8 \text{ mJy beam}^{-1}$. The dashed circle in both panels is centred on the cluster and has a radius of 1 Mpc.

4.1. Contaminating and blended sources

The MWA in Phase I has a reasonably low angular resolution when compared to telescopes such as the VLA, GMRT, ATCA, or WRST¹⁰. This is a limitation that arises simply due to the lack of baselines greater than 2873.3 m (in Phase I) and its low observing frequency. Without follow-up observations with higher-resolution instruments it becomes difficult to confirm the nature of emission we find here due to source blending and embedded discrete radio sources or faint point source populations. Two main confusing cases may arise: (i) a source detected at 168 MHz has no counterpart in other survey images, or (ii) an apparently extended source at 168 MHz corresponds to extended sources in other images.

(i) A non-detection of a point source with the TGSS ADR1 data with ~ 25 arcsec resolution provides some confidence in the emission being extended rather than made up of blended point sources. While the sensitivity of the TGSS ADR1 ($\gtrsim 3.5 \text{ mJy beam}^{-1}$) does limit the information we get from a non-detection, it does allow us to consider whether a faint source population could reasonably explain the 168-MHz emission. As an example, consider that Abell 2693 would require a faint population of point sources with a total flux density of $S_{150} \sim 56 \text{ mJy}$. This would require ~ 5 discrete sources (unconfused at the TGSS resolution) within an emission area smaller than the MWA beam, which is not possible. Certainly, a portion of the emission may be made up of a faint point source population, but some residual emission must remain.

(ii) This case is more difficult to confirm, however, a deficit in flux between the MWA and TGSS ADR1 data would pro-

vide insight into whether there is an extended, low surface-brightness component associated with the emission which may provide support for the existence of diffuse cluster emission. This requires careful measurement of flux densities to have any practical value, and as we near the respectively noise levels in each image this becomes prohibitively more difficult to confirm. Additionally, any difference in flux scale will hinder such an approach¹¹.

In future work with the MWA, a test for the compact nature of emission may be possible through the interplanetary scintillation (IPS; see Morgan et al., 2018; Chhetri et al., 2018). Specifically, Chhetri et al. (2018) show that extended, diffuse sources with steep spectral indices (e.g. the relic in Abell 0085) have low scintillation indices that preclude their emission from being dominated by compact sources. At present, these IPS observations do not reach the required sensitivity to detect most sources in this paper. Making use of these techniques in the future may alleviate some of the issues surrounding low-resolution radio imaging and source-blending.

4.2. The scaling relations of cluster radio haloes

4.2.1. The $P_{1.4-L_X}$ and $P_{1.4}-M_{500}$ relations

An empirical relation exists between the thermal and non-thermal emission of galaxy clusters traced by the syn-

¹⁰Westerbork Synthesis Radio Telescope

¹¹Noting also a known systematic flux scale discrepancy between TGSS ADR1 and MWA data: <http://tgssadr.strw.leidenuniv.nl/doku.php?id=knownproblems>

¹²Adapted from <https://github.com/rsnemmen/nemmen/blob/master/nemmen/stats.py>

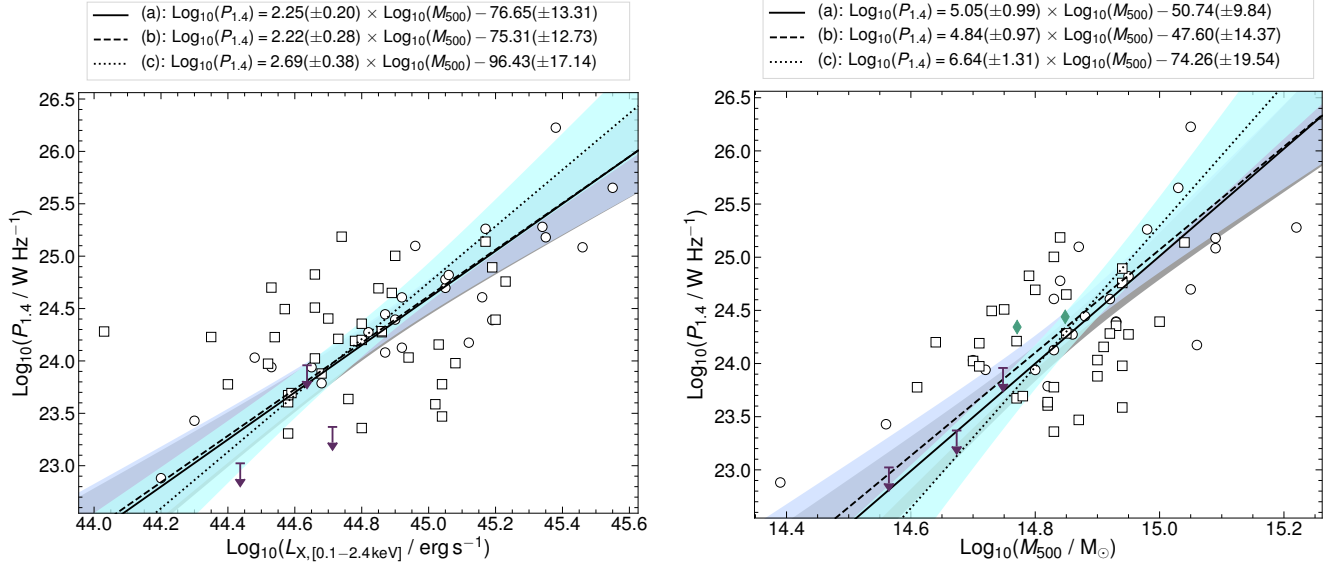


Figure 27. *Left:* The $P_{1.4}$ – L_X scaling relation. *Right:* The $P_{1.4}$ – M_{500} scaling relation. Error bars have been omitted for the sake of clarity. Unfilled markers are for clusters hosting haloes from the literature. Circles represent those clusters with measured spectral indices, and squares are those assumed to have the average spectral index $\langle \alpha \rangle = -1.47 \pm 0.30$. The dark-purple upper limits are from haloes presented in this paper. The green diamonds are for haloes in GMBCG J357.91841–08.97978 and Abell S1121. The fits presented are from (a) Cassano et al. (2013) and (b)/(c) this work—see text for details. The shaded regions represent 95% confidence intervals ¹².

chrotron emission 1.4 GHz power, $P_{1.4}$, and the thermal Bremsstrahlung X-ray luminosity, L_X . The $P_{1.4}$ – L_X scaling relations have been updated with new surveys halo detections (e.g. GRHS: I; Venturi et al. 2007 and II; Venturi et al. 2008, EGRHS ¹³: I; Kale et al. 2013 and II; Kale et al. 2015, KAT-7 observations: Bernardi et al. 2016, ARDES: I; Shakouri et al. 2016) to try to understand the link between the thermal X-ray-emitting plasma and radio-halo-emitting electron population and the link to the dynamical state of the cluster (e.g. Cassano et al., 2007). Additional relationships between radio halo power and the cluster’s SZ effect with $P_{1.4}$ – Y_{SZ} (Basu, 2012) and SZ-derived mass $P_{1.4}$ – $M_{\text{YZ},500}$ (Cassano et al., 2013, but see also Arnaud et al. 2010) also exist.

We compare our newly detected halo/candidate haloes (that have required mass and X-ray luminosities) with the literature sample of haloes (as of July 2017). We consider the following results in the event the emission within Abell S1121 is a radio halo. For haloes not measured at 1.4 GHz we extrapolate the flux density measurements to 1.4 GHz using measured spectral indices where available or assuming a spectral index of $\alpha = -1.47 \pm 0.30$ which is the average of the measured indices. We then determine a k -corrected $P_{1.4}$ (see Hogg, 1999; Hogg et al., 2002) via

$$P_{1.4} = \frac{4\pi D_L^2(z)}{(1+z)^{1+\alpha}} S_{1.4} \quad [\text{W Hz}^{-1}], \quad (3)$$

with the luminosity distance, $D_L(z)$, at the cluster’s redshift,

and associated error, $\sigma_{P_{1.4}}$,

$$\sigma_{P_{1.4}} = \frac{P_{1.4}}{S_{1.4}} \sqrt{[S_{1.4} \ln(1+z) \sigma_{\alpha}]^2 + (\sigma_{S_{1.4}})^2} \quad [\text{W Hz}^{-1}]. \quad (4)$$

Clusters used here from the literature with radio haloes are presented in Appendix A. From here, we consider two radio halo samples: those with measured spectral indices and the full sample. Fig. 27 shows the $P_{1.4}$ – L_X (left panel) and $P_{1.4}$ – M_{500} (right panel) relations, with the global sample of clusters as well as clusters from this work with upper limits (dark purple) and exact radio halo powers (green diamonds in the right panel). In Fig. 27, clusters represented with a circle are those with a measured spectral index and squares are those assuming an average spectral index of $\langle \alpha \rangle = -1.47 \pm 0.30$. Fig. 27 also shows the best-fitting orthogonal BCES ¹⁴ linear regression lines to both relations presented by Cassano et al. (2013) (solid line). Additionally, we fit each sample (measured α only and all haloes) via the same method. These fits are shown as dashed and dotted lines, respectively.

We find that some of the haloes in our newly detected sample lie below the $P_{1.4}$ – L_X relation and above the $P_{1.4}$ – M_{500} relation. In particular, Abell 2811 and Abell 0141 sit below the $P_{1.4}$ – L_X relation, though still fall within the general scatter of the remaining cluster radio halo locations. Though their locations are upper limits, and they may lie even further below if their powers are lower. Similarly, GMBCG J357.91841–08.97978 lies above the $P_{1.4}$ – M_{500} relation.

¹³Extended GMRT Radio Halo Survey

¹⁴Bivariate Correlated Errors and intrinsic Scatter, (Akritas & Bershady, 1996)

Table 6 Raw scatter between cluster halo samples with best-fitting BCES regression lines to the scaling relations by (a) Cassano et al. (2013) and (b) this work.

Ref.	a^a	b^a	Sample	σ_{raw}
$P_{1.4}-L_X$				
(a)	2.25 ± 0.25	-76.65 ± 13.31	Full	0.393
			α	0.305
(b)	2.69 ± 0.38	-96.43 ± 17.14	Full	0.423
	2.22 ± 0.28	-75.31 ± 12.73	α	0.299
$P_{1.4}-M_{500}$				
(a)	5.05 ± 0.99	-50.74 ± 9.84	Full	0.594
			α	0.536
(b)	6.64 ± 1.31	-74.26 ± 19.54	Full	0.771
	4.84 ± 0.97	-47.60 ± 14.37	α	0.550

^a For $\log_{10}(P_{1.4}) = a \log_{10}(X) + b$ for $X \in \{L_X, M_{500}\}$.

4.2.2. Comparing the scaling relations

We compare the robustness of the $P_{1.4}-L_X$ and $P_{1.4}-M_{500}$ relations using a measure of the raw scatter, σ_{raw} , of the best-fitting BCES regression lines from Cassano et al. (2013) and this work. The raw scatter is calculated as the error-weighted orthogonal distances to the best-fitting regression line via (e.g. Pratt et al., 2009; Cassano et al., 2013)

$$\sigma_{\text{raw}}^2 = \frac{N}{(N-2) \sum_{i=1}^N 1/\sigma_i^2} \sum_{i=1}^N \frac{1}{\sigma_i^2} (Y_i - aX_i - b), \quad (5)$$

where N is the sample size, $\sigma_i^2 = \sigma_{y_i}^2 + a^2 \sigma_{x_i}^2$ for uncertainties σ_y , σ_x in Y , X , and fitting parameters a , b .

Table 6 presents the calculated raw scatter in each fit for each of the samples. We see clearly that the measured α sample shows considerably less scatter in all cases, though is also the smaller sample. The sample size from Cassano et al. (2013) is 25 haloes, while the full sample used here is 63(59) and the measured α sample is 25(24) for $P_{1.4}-L_X$ ($P_{1.4}-M_{500}$).

Pratt et al. (2009) find, for a representative sample of clusters, that the X-ray luminosities show more scatter when cool core clusters are in the sample. Fig. 28 shows the L_X-M_{500} relation for clusters hosting radio haloes (literature and this work). The solid, black fit with mauve 95% confidence region is a BCES orthogonal fit to the cluster hosting haloes, whereas the dotted and dashed, black fits (for $z = 1$ and $z = 0$) are the equivalent BCES orthogonal fits presented by Pratt et al. (2009) for the REXCESS sample of clusters, which comprises both cool and non-cool core clusters. The blue, down-pointing triangles indicate clusters with L_X below their values predicted by the REXCESS sample and red, up-pointing triangles are with L_X above predicted values. The six clusters above their predicted L_X are: CL 1821+643, Abell 1914, Abell 0545, Abell 3562, and RXC J1314.4–2512. We note that CL 1821+643 hosts a cool core and features a giant radio halo with LLS of ~ 1.1 Mpc (Bonafede et al., 2014). Abell 3562 hosts a cooling flow (Peres et al., 1998)

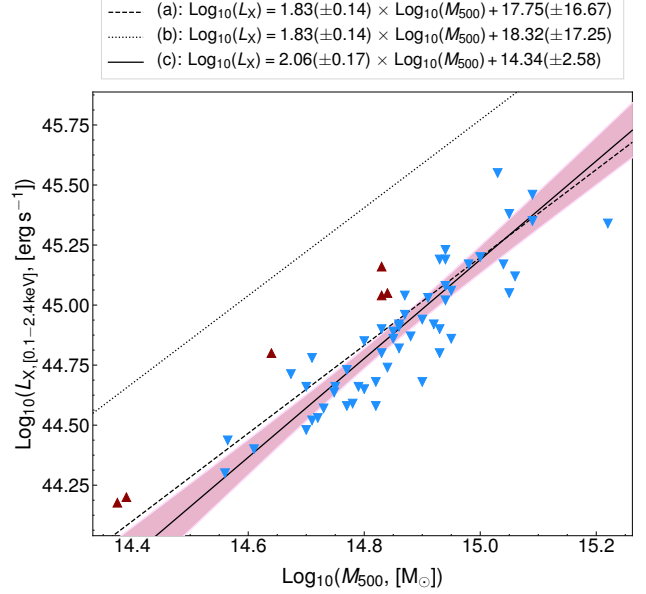


Figure 28. X-ray luminosity against mass for clusters hosting radio haloes. The solid, black fit (c) is made using the BCES orthogonal method for clusters with haloes with the mauve shaded region the 95% confidence interval as per Fig. 27. The dashed, black fit (a) is from Pratt et al. (2009) for clusters within the REXCESS sample using the same BCES orthogonal fitting method, assuming a redshift of 0. The dotted, black fit (b) is the same fit from Pratt et al. but assuming a redshift of 1. The red, up-pointing triangles indicate clusters with predicted L_X below measured values, and blue, down-pointing triangles are clusters with predicted L_X above measured values. This sample is the global sample with the addition of the clusters found to host haloes (or candidates) from this work.

and the lowest-power halo in the global sample (Venturi et al., 2003; Giovannini et al., 2009a) and also features the second-lowest mass and lowest luminosity cluster. The remaining three clusters are described as disturbed or dynamically active: Abell 1914 has no cooling flow (White, 2000) and a morphological analysis performed by Buote & Tsai (1996) suggests a dynamical nature; Abell 0545 has an unrelaxed and highly elongated X-ray structure (Bacchi et al., 2003); RXC J1314.4–2512 is dynamically perturbed with bi-modal structure and odd elongation (Valtchanov et al., 2002).

The sample of clusters used by Pratt et al. (2009) feature $\sim 32\%$ cool cores, which in the L_X-T relation preferentially lie above the best-fitting parameters. With a significant lack of cool core clusters, we find best-fitting parameters to the L_X-M_{500} relation that shows a slightly steeper slope. There is only one cool-core cluster known to host a radio halo (CL 1821+643) and this may explain the lower scatter in the $P_{1.4}-L_X$ relation compared to that in the $P_{1.4}-M_{500}$ relation, where we would otherwise expect a relation derived from homogeneous mass measurements to be more tightly constrained than that of inhomogeneous X-ray measurements. Simulations show that there may be a transient boost to L_X during the course of a cluster merger (Donnert et al., 2013), though it is not clear whether this will push the cluster above the $P_{1.4}-L_X$ relation or along it with a simultaneous increase

to the radio halo power. Less scatter in the $P_{1.4}$ - L_X relation may suggest the latter, where transient boosts above the relation would otherwise increase the raw scatter.

A significant contribution to raw scatter in the data (which exists for both $P_{1.4}$ - L_X and $P_{1.4}$ - M_{500} relations) may arise from inhomogeneous $P_{1.4}$ measurements and determination of α . Radio flux densities are often measured on maps made with differing beam sizes and u - v plane coverage. In the case of missing u - v coverage, not all spatial scales are recovered which results in missing flux, yielding lower limits to integrated flux densities. Additionally, there is no single method used for measuring flux density (see e.g. Sommer & Basu, 2014). Flux densities are not always measured at 1.4 GHz, and sometimes—as in this work—a lower-frequency integrated flux density is measured for the halo, and a corresponding 1.4 GHz flux density (hence, power) is extrapolated from a calculated or assumed spectral index. The integrated spectral index itself may introduce additional scatter without a well-sampled spectrum. It is typical to assume a spectral index of -1.3 (e.g. Cassano et al., 2013), though here we use -1.47 which is found to be the mean value of the measured spectral indices. Even haloes measured at 1.4 GHz require an accurate determination of the spectral index as it is important for the k -correction in calculating $P_{1.4}$ as $P_{1.4} \propto 1/(1+z)^{1+\alpha}$. This can result in a $\sim 20\%$ difference at $z = 0.2$ between $\alpha = -1$ and $\alpha = -2$.

4.3. The incidence of diffuse cluster emission within the EoR0 field

This work presents a number of new haloes, relics, and phoenixes or candidates of each along with previously objects previously detected. Given the resolution of the EoR0 field (or its approximate beam size) of ~ 2.3 arcmin, we can estimate the limits in mass and redshift for detecting radio haloes and relics using the $P_{1.4}$ - M_{500} scaling relations of Cassano et al. (2013; for haloes) and de Gasperin et al. (2014; for relics). We do not consider the detection limit for phoenixes as no scaling relations exist for these objects.

The two major limiting factors in the detection of such emission are the resolution and sensitivity of the telescope. With the EoR0 field's approximate beam size of ~ 2.3 arcmin, the viable detection range for distant haloes is $z \leq 0.22$ for $LLS \leq 500$ kpc or $z \leq 0.67$ for $LLS \leq 1000$ kpc. Beyond this, haloes become point sources. The second issue is sensitivity; the EoR0 field reaches a sensitivity of approximately 2.3 mJy beam $^{-1}$ in the central regions of the image. The lowest theoretical sensitivity of the Phase I MWA is approximately 1.7 mJy beam $^{-1}$ (Franzen et al., 2016). With the redshift limits above for the 500 and 1000 kpc radio haloes (or relics, as the argument is the same when approaching the beamsize) the sensitivity is not the major limiting factor. If we assume the smallest-power halo can be detected at > 6.9 mJy, and if we assume $\alpha = -1.47$ that goes into the k -correction, then the limits on detectable radio halo power are $P_{1.4}(z = 0.22) \geq 0.7 \times 10^{23}$ and $P_{1.4}(z = 0.67) \geq 10 \times 10^{23}$ W Hz $^{-1}$.

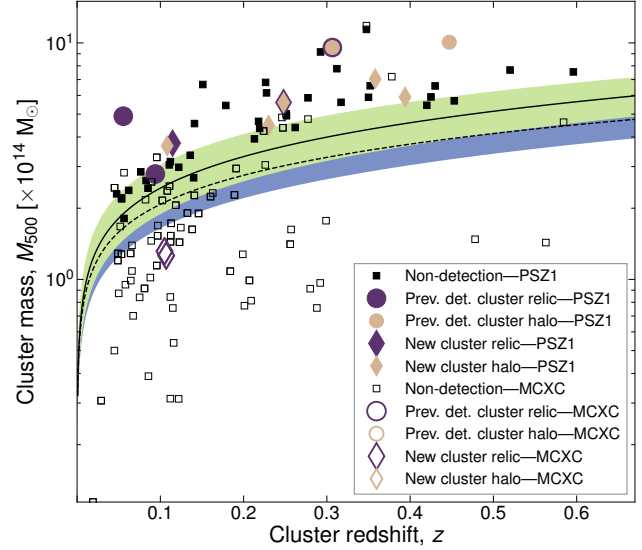


Figure 29. Cluster mass against redshift for clusters within the MCXC and PSZ1 catalogues. The filled points are those using the PSZ1 $M_{YZ,500}$ measurements and unfilled points are those using the MCXC M_{500} measurements. Where clusters appear in both catalogues we use the PSZ1 $M_{YZ,500}$ measurements. The olive-green and blue shaded regions indicate the limits at which 1 Mpc haloes or relics can be detected given the $P_{1.4}$ - M_{500} scaling relations found by Cassano et al. (2013) and de Gasperin et al. (2014), respectively. These are determined assuming a $3\sigma_{\text{rms}}$ detection of 3×2.3 mJy beam $^{-1}$, beam size of 2.3 arcmin, and spectral indices between $-0.9 \leq \alpha \leq -2.1$, where a steeper spectral index requires a lower mass cluster. The solid and dashed curves indicate limits for $\alpha = -1.47$ for haloes and relics, respectively.

This entire range falls below what is typically seen of cluster haloes (e.g. Cassano et al., 2013; Kale et al., 2015; Shakouri et al., 2016).

Fig. 29 shows clusters within the MCXC and PSZ1 catalogue located within the EoR0 field plotting mass against redshift. We indicate clusters hosting haloes and/or relics—both previously detected and those detected as part of this work. We use the scaling relations of Cassano et al. (2013; for haloes) and de Gasperin et al. (2014; for relics) to determine the detection limits of these objects within the EoR0 field. For these detection limits, we assume a limiting flux density of 6.9 mJy (the minimum $3\sigma_{\text{rms}}$ for the field) and extrapolate to $P_{1.4}$ for the redshift range $0 \leq z \leq 0.67$ assuming a range of spectral indices $-0.9 \leq \alpha \leq -2.1$. These limiting $P_{1.4}$ values are used with the aforementioned $P_{1.4}$ - M_{500} scaling relations to estimate the required mass for a given $P_{1.4}$. These detection limits are plotted as shaded regions with lines drawn at $\alpha = -1.47$. The halo limit region is better defined as the assumption on source size is for a beam-shaped halo, relics typically have shallow spectral indices (Feretti et al., 2012), and because the $P_{1.4}$ - M_{500} relation for haloes is better defined with a larger sample and less scatter. The newly detected relic in Abell 2751 and the candidate in Abell 2798 lie below the $-0.9 \leq \alpha \leq -2.1$ shaded region for relic detections. For the clusters plotted in Fig. 29, $\sim 37\%$ lie above the derived

1 Mpc, $\alpha = -1.47$ halo detection limit and $\sim 45\%$ lie above the corresponding detection limit for relics.

5. Summary

We have presented diffuse cluster emission detected by the MWA at 168 MHz within the $45^\circ \times 45^\circ$ EoR0 field including numerous candidates. The field is searched by eye, focusing on clusters part of the Abell, MCXC, PSZ1 galaxy cluster catalogues with reported redshifts. We report the following cluster-based sources:

1. 9 halos and candidate halos, including mini-halo sources, of which 2 are known.
2. 7 relics and candidate relics, of which 2 are known.
3. 4 known phoenixes and 1 candidate phoenix.
4. 9 sources in clusters with similar features to the above which we cannot classify easily within the current taxonomy.

Where possible, we measure 168 MHz flux densities, estimate angular and linear sizes, and estimate spectral indices or spectral index limits based on non-detections at other frequencies. In particular, we detect a halo associated with the cluster Abell 0141 which is undergoing a merger as suggested by the bi-modality of the galaxy distribution and X-ray-emitting plasma. This halo appears to have an ultra-steep spectrum with $\alpha_{168}^{610} \leq -2.1 \pm 0.1$. Such ultra-steep-spectrum haloes are predicted to be found in low-frequency surveys (Cassano et al., 2012) and their detection is suggestive of the validity of current halo acceleration models.

We consider the impact of the MWA's resolution on its ability to properly measure the flux density of sources and its ability to unambiguously confirm the nature of seemingly extended emission, concluding that for the EoR0, the TGSS works well to check for the worst point source contamination, but higher-resolution followups would be needed for cases where source blending may be at play. We examine the newly detected haloes within the context of the established $P_{1.4}-L_X$ and $P_{1.4}-M_{500}$ scaling relations, finding their locations fairly consistent with other cluster-hosted haloes. We examine previously-found best-fitting relations and derive new fits based on a literature sample and new halo detections.

We find that radio haloes are predominantly hosted by clusters below the established L_X-M_{500} relation for clusters from the REXCESS sample, with only four examples above the relation not hosting cool cores. Finally, with these new halo and relic detections we examine the incidence of such emission, finding that the MWA is beginning to see emission with little bias beyond what is present in the catalogues the clusters are drawn from.

Acknowledgements. The authors would like to thank Emil Lenc, Thomas Reiprich, Tiziana Venturi, Francesco de Gasperin, and Susannah R. Keel for their help in preparation of this paper. We would also like to thank two anonymous referees for their valuable comments that have improved this paper. SWD, MJ-H, and QZ acknowledge the Marsden Fund administered by the Royal Society of

New Zealand. SWD also acknowledges a Doctoral Scholarship from Victoria University of Wellington and Australian Government Research Training Programme scholarship administered through Curtin University. This scientific work makes use of the Murchison Radio-astronomy Observatory, operated by CSIRO. We acknowledge the Wajarri Yamatji people as the traditional owners of the Observatory site. Support for the operation of the MWA is provided by the Australian Government (NCRIS), under a contract to Curtin University administered by Astronomy Australia Limited. We acknowledge the Pawsey Supercomputing Centre which is supported by the Western Australian and Australian Governments.

This research made use of `astropy` (Astropy Collaboration et al., 2013), `aplpy` (<http://aplpy.github.com>), `NumPy` (van der Walt et al., 2011), `matplotlib` (Hunter, 2007), `iPython` (Pérez & Granger, 2007) and the `SciPy` library (<https://www.scipy.org/>). This research has made use of the VizieR catalogue access tool, CDS, Strasbourg, France. The original description of the VizieR service was described in Ochsenbein et al. (2000). This research also made use of the NASA/IPAC Extragalactic Database (NED) which is operated by the Jet Propulsion Laboratory, California Institute of Technology, under contract with the National Aeronautics and Space Administration. The Digitized Sky Surveys were produced at the Space Telescope Science Institute under U.S. Government grant NAG W-2166. The images of these surveys are based on photographic data obtained using the Oschin Schmidt Telescope on Palomar Mountain and the UK Schmidt Telescope. The plates were processed into the present compressed digital form with the permission of these institutions.

References

- Abbott T. M. C., et al., 2018, *ApJS*, **239**, 18
 Abell G. O., 1958, *ApJS*, **3**, 211
 Abell G. O., Corwin Jr. H. G., Olowin R. P., 1989, *ApJS*, **70**, 1
 Ackermann M., et al., 2014, *ApJ*, **787**, 18
 Akritas M. G., Bershadsky M. A., 1996, *ApJ*, **470**, 706
 Ananthakrishnan S., 1995, *Journal of Astrophysics and Astronomy Supplement*, **16**, 427
 Arnaud M., Pratt G. W., Piffaretti R., Böhringer H., Croston J. H., Pointecouteau E., 2010, *A&A*, **517**, A92
 Astropy Collaboration et al., 2013, *A&A*, **558**, A33
 Baars J. W. M., Genzel R., Pauliny-Toth I. I. K., Witzel A., 1977, *A&A*, **61**, 99
 Bacchi M., Feretti L., Giovannini G., Govoni F., 2003, *A&A*, **400**, 465
 Bagchi J., Durret F., Neto G. B. L., Paul S., 2006, *Science*, **314**, 791
 Basu K., 2012, *MNRAS*, **421**, L112
 Bernardi G., et al., 2016, *MNRAS*, **456**, 1259
 Blasi P., Colafrancesco S., 1999, *Astroparticle Physics*, **12**, 169
 Bock D. C.-J., Large M. I., Sadler E. M., 1999, *AJ*, **117**, 1578
 Böhringer H., et al., 2004, *A&A*, **425**, 367
 Böhringer H., et al., 2007, *A&A*, **469**, 363
 Bonafede A., et al., 2009, *A&A*, **503**, 707
 Bonafede A., Feretti L., Murgia M., Govoni F., Giovannini G., Dallacasa D., Dolag K., Taylor G. B., 2010, *A&A*, **513**, A30
 Bonafede A., et al., 2012, *MNRAS*, **426**, 40
 Bonafede A., et al., 2014, *MNRAS*, **444**, L44
 Bonafede A., et al., 2015, *MNRAS*, **454**, 3391
 Bowman J. D., et al., 2013, *PASA*, **30**, 31
 Bravi L., Gitti M., Brunetti G., 2016, *MNRAS*, **455**, L41
 Bridle A. H., Fomalont E. B., Miley G. K., Valentijn E. A., 1979, *A&A*, **80**, 201

- Briggs D. S., 1995, in American Astronomical Society Meeting Abstracts, p. 1444
- Brown S., Duesterhoeft J., Rudnick L., 2011, *ApJ*, **727**, L25
- Brunetti G., Blasi P., 2005, *MNRAS*, **363**, 1173
- Brunetti G., Jones T. W., 2014, *International Journal of Modern Physics D*, **23**, 1430007
- Brunetti G., Lazarian A., 2011, *MNRAS*, **412**, 817
- Brunetti G., Lazarian A., 2016, *MNRAS*, **458**, 2584
- Brunetti G., Setti G., Feretti L., Giovannini G., 2001, *MNRAS*, **320**, 365
- Brunetti G., et al., 2008, *Nature*, **455**, 944
- Buote D. A., 2001, *ApJ*, **553**, L15
- Buote D. A., Tsai J. C., 1996, *ApJ*, **458**, 27
- Caglar T., 2018, *MNRAS*, **475**, 2870
- Cantwell T. M., Scaife A. M. M., Oozeer N., Wen Z. L., Han J. L., 2016, *MNRAS*, **458**, 1803
- Caretta C. A., Maia M. A. G., Kawasaki W., Willmer C. N. A., 2002, *AJ*, **123**, 1200
- Caretta C. A., Maia M. A. G., Willmer C. N. A., 2004, *AJ*, **128**, 2642
- Cassano R., Brunetti G., Setti G., 2006, *MNRAS*, **369**, 1577
- Cassano R., Brunetti G., Setti G., Govoni F., Dolag K., 2007, *MNRAS*, **378**, 1565
- Cassano R., Brunetti G., Norris R. P., Röttgering H. J. A., Johnston-Hollitt M., Trasatti M., 2012, *A&A*, **548**, A100
- Cassano R., et al., 2013, *ApJ*, **777**, 141
- Castellano M., et al., 2016, *A&A*, **590**, A31
- Chambers K. C., et al., 2016, preprint, ([arXiv:1612.05560](https://arxiv.org/abs/1612.05560))
- Chhetri R., Morgan J., Ekers R. D., Macquart J.-P., Sadler E. M., Giroletti M., Callingham J. R., Tingay S. J., 2018, *MNRAS*, **474**, 4937
- Chon G., Böhringer H., 2012, *A&A*, **538**, A35
- Clarke T. E., Ensslin T. A., 2006, *AJ*, **131**, 2900
- Clarke T. E., Kronberg P. P., Böhringer H., 2001, *ApJ*, **547**, L111
- Cohen A. S., Clarke T. E., 2011, *AJ*, **141**, 149
- Condon J. J., Cotton W. D., Greisen E. W., Yin Q. F., Perley R. A., Taylor G. B., Broderick J. J., 1998, *AJ*, **115**, 1693
- Coziol R., Andernach H., Caretta C. A., Alamo-Martínez K. A., Tago E., 2009, *AJ*, **137**, 4795
- Cuciti V., Brunetti G., van Weeren R., Bonafede A., Dallacasa D., Cassano R., Venturi T., Kale R., 2018, *A&A*, **609**, A61
- Dahle H., Kaiser N., Irgens R. J., Lilje P. B., Maddox S. J., 2002, *ApJS*, **139**, 313
- Dalton G. B., Maddox S. J., Sutherland W. J., Efstathiou G., 1997, *MNRAS*, **289**, 263
- Dennison B., 1980, *ApJ*, **239**, L93
- Diego J. M., Broadhurst T., Wong J., Silk J., Lim J., Zheng W., Lam D., Ford H., 2016, *MNRAS*, **459**, 3447
- Dolag K., Enßlin T. A., 2000, *A&A*, **362**, 151
- Donnert J., Dolag K., Brunetti G., Cassano R., 2013, *MNRAS*, **429**, 3564
- Ebeling H., Edge A. C., Henry J. P., 2001, *ApJ*, **553**, 668
- Ebeling H., Edge A. C., Mantz A., Barrett E., Henry J. P., Ma C. J., van Speybroeck L., 2010, *MNRAS*, **407**, 83
- Enßlin T. A., Brüggem M., 2002, *MNRAS*, **331**, 1011
- Enßlin T. A., Gopal-Krishna 2001, *A&A*, **366**, 26
- Farnsworth D., Rudnick L., Brown S., Brunetti G., 2013, *ApJ*, **779**, 189
- Feretti L., Fusco-Femiano R., Giovannini G., Govoni F., 2001, *A&A*, **373**, 106
- Feretti L., Orrù E., Brunetti G., Giovannini G., Kassim N., Setti G., 2004, *A&A*, **423**, 111
- Feretti L., Giovannini G., Govoni F., Murgia M., 2012, *A&A Rev.*, **20**, 54
- Finlay E. A., Jones B. B., 1973, *Australian Journal of Physics*, **26**, 389
- Flaugher B., et al., 2015, *AJ*, **150**, 150
- Franzen T. M. O., et al., 2016, *MNRAS*, **459**, 3314
- Frater R. H., Brooks J. W., Whiteoak J. B., 1992, *Journal of Electrical and Electronics Engineering Australia*, **12**, 103
- Fujita Y., Sarazin C. L., Kempner J. C., Rudnick L., Slee O. B., Roy A. L., Andernach H., Ehle M., 2002, *ApJ*, **575**, 764
- Fujita Y., Sarazin C. L., Reiprich T. H., Andernach H., Ehle M., Murgia M., Rudnick L., Slee O. B., 2004, *ApJ*, **616**, 157
- George L. T., et al., 2017, *MNRAS*, **467**, 936
- Giacintucci S., et al., 2005, *A&A*, **440**, 867
- Giacintucci S., Venturi T., Brunetti G., Dallacasa D., Mazzotta P., Cassano R., Bardelli S., Zucca E., 2009, *A&A*, **505**, 45
- Giacintucci S., Dallacasa D., Venturi T., Brunetti G., Cassano R., Markevitch M., Athreya R. M., 2011, *A&A*, **534**, A57
- Giacintucci S., Kale R., Wik D. R., Venturi T., Markevitch M., 2013, *ApJ*, **766**, 18
- Giovannini G., Feretti L., 2000, *New Astronomy*, **5**, 335
- Giovannini G., Tordi M., Feretti L., 1999, *New Astronomy*, **4**, 141
- Giovannini G., Bonafede A., Feretti L., Govoni F., Murgia M., Ferrari F., Monti G., 2009a, *A&A*, **507**, 1257
- Giovannini G., Bonafede A., Feretti L., Govoni F., Murgia M., Ferrari F., Monti G., 2009b, *A&A*, **507**, 1257
- Girardi M., et al., 2016, *MNRAS*, **456**, 2829
- Govoni F., Feretti L., Giovannini G., Böhringer H., Reiprich T. H., Murgia M., 2001, *A&A*, **376**, 803
- Govoni F., Murgia M., Feretti L., Giovannini G., Dallacasa D., Taylor G. B., 2005, *A&A*, **430**, L5
- Govoni F., Murgia M., Giovannini G., Vacca V., Bonafede A., 2011, *A&A*, **529**, A69
- Govoni F., Ferrari C., Feretti L., Vacca V., Murgia M., Giovannini G., Perley R., Benoist C., 2012, *A&A*, **545**, A74
- Govoni F., Murgia M., Xu H., Li H., Norman M. L., Feretti L., Giovannini G., Vacca V., 2013, *A&A*, **554**, A102
- Green D. A., 2011, *Bulletin of the Astronomical Society of India*, **39**, 289
- Guzzo L., et al., 2009, *A&A*, **499**, 357
- Hales C. A., Murphy T., Curran J. R., Middelberg E., Gaensler B. M., Norris R. P., 2012, *MNRAS*, **425**, 979
- Hancock P. J., Murphy T., Gaensler B. M., Hopkins A., Curran J. R., 2012, *MNRAS*, **422**, 1812
- Hao J., et al., 2010, *ApJS*, **191**, 254
- Henley D. B., Shelton R. L., 2013, *ApJ*, **773**, 92
- Hindson L., et al., 2014, *MNRAS*, **445**, 330
- Hogg D. W., 1999, preprint, ([arXiv:astro-ph/9905116](https://arxiv.org/abs/astro-ph/9905116))
- Hogg D. W., Baldry I. K., Blanton M. R., Eisenstein D. J., 2002, preprint, ([arXiv:astro-ph/0210394](https://arxiv.org/abs/astro-ph/0210394))
- Hollitt C., Johnston-Hollitt M., 2012, *PASA*, **29**, 309
- Hunter J. D., 2007, *Computing in Science & Engineering*, **9**, 90
- Intema H. T., Jagannathan P., Mooley K. P., Frail D. A., 2017, *A&A*, **598**, A78
- Johnston-Hollitt M., 2003, PhD thesis, University of Adelaide
- Johnston-Hollitt M., 2017, *Nature Astronomy*, **1**, 0014
- Kaiser N., et al., 2010, in *Ground-based and Airborne Telescopes III*. p. 77330E, doi:10.1117/12.859188
- Kale R., Dwarakanath K. S., 2012, *ApJ*, **744**, 46
- Kale R., Parekh V., 2016, *MNRAS*, **459**, 2940
- Kale R., Venturi T., Giacintucci S., Dallacasa D., Cassano R., Brunetti G., Macario G., Athreya R., 2013, *A&A*, **557**, A99
- Kale R., et al., 2015, *A&A*, **579**, A92
- Kapińska A. D., et al., 2017, *ApJ*, **838**, 68
- Kempner J. C., Sarazin C. L., Ricker P. M., 2002, *ApJ*, **579**, 236
- Kempner J. C., Blanton E. L., Clarke T. E., Enßlin T. A., Johnston-Hollitt M., Rudnick L., 2004, in Reiprich T., Kempner J., Soker N., eds, *The Riddle of Cooling Flows in Galaxies and Clusters of galaxies*. ([arXiv:astro-ph/0310263](https://arxiv.org/abs/astro-ph/0310263))
- Kim K.-T., Kronberg P. P., Dewdney P. E., Landecker T. L., 1990, *ApJ*, **355**, 29
- Knowles K., et al., 2016, *MNRAS*, **459**, 4240
- Komissarov S. S., Gubanov A. G., 1994, *A&A*, **285**, 27
- Lane W. M., Cotton W. D., van Velzen S., Clarke T. E., Kassim N. E., Helmboldt J. F., Lazio T. J. W., Cohen A. S., 2014, *MNRAS*, **440**, 327
- Leir A. A., van den Bergh S., 1977, *ApJS*, **34**, 381
- Liang H., Hunstead R. W., Birkinshaw M., Andreani P., 2000, *ApJ*, **544**, 686
- Liang H., Ekers R. D., Hunstead R. W., Falco E. E., Shaver P., 2001, *MNRAS*,

- 328, L21
- Liang Y.-F., et al., 2016, *Phys. Rev. D*, **93**, 103525
- Lindner R. R., et al., 2014, *ApJ*, **786**, 49
- Liu J., et al., 2015, *MNRAS*, **449**, 3370
- Lotz J. M., et al., 2017, *ApJ*, **837**, 97
- Markevitch M., 2006, in Wilson A., ed., *ESA Special Publication Vol. 604, The X-ray Universe 2005*. p. 723 ([arXiv:astro-ph/0511345](https://arxiv.org/abs/astro-ph/0511345))
- Martinez Aviles G., et al., 2016, *A&A*, **595**, A116
- Mauch T., Murphy T., Buttery H. J., Curran J., Hunstead R. W., Piestrzynski B., Robertson J. G., Sadler E. M., 2003, *MNRAS*, **342**, 1117
- Morgan J. S., et al., 2018, *MNRAS*, **473**, 2965
- Morganson E., et al., 2018, *PASP*, **130**, 074501
- Murgia M., Govoni F., Feretti L., Giovannini G., 2010, *A&A*, **509**, A86
- Ochsenbein F., Bauer P., Marcout J., 2000, *A&AS*, **143**, 23
- Oegerle W. R., Hill J. M., 2001, *AJ*, **122**, 2858
- Offringa A. R., et al., 2016, *MNRAS*, **458**, 1057
- Ogrean G. A., et al., 2015, *ApJ*, **812**, 153
- Owen F. N., Ledlow M. J., Keel W. C., 1995, *AJ*, **109**, 14
- Parekh V., Dwarakanath K. S., Kale R., Intema H., 2017, *MNRAS*, **464**, 2752
- Peebles P. J. E., 1980, *The large-scale structure of the universe*. Princeton Univ. Press, Princeton, N. J.
- Peres C. B., Fabian A. C., Edge A. C., Allen S. W., Johnstone R. M., White D. A., 1998, *MNRAS*, **298**, 416
- Pérez F., Granger B. E., 2007, *Computing in Science & Engineering*, **9**, 21
- Petrosian V., 2001, *ApJ*, **557**, 560
- Petrosian V., East W. E., 2008, *ApJ*, **682**, 175
- Piffaretti R., Arnaud M., Pratt G. W., Pointecouteau E., Melin J.-B., 2011, *A&A*, **534**, A109
- Pimblet K. A., Smail I., Edge A. C., O’Hely E., Couch W. J., Zabludoff A. I., 2006, *MNRAS*, **366**, 645
- Planck Collaboration et al., 2014, *A&A*, **571**, A29
- Planck Collaboration et al., 2015, *A&A*, **581**, A14
- Pratt G. W., Croston J. H., Arnaud M., Böhringer H., 2009, *A&A*, **498**, 361
- Prokhorov D. A., Churazov E. M., 2014, *A&A*, **567**, A93
- Rajpurohit K., et al., 2020, *A&A*, **642**, L13
- Randall S. W., Clarke T. E., Nulsen P. E. J., Owers M. S., Sarazin C. L., Forman W. R., Murray S. S., 2010, *ApJ*, **722**, 825
- Reichert G., Mason K. O., Charles P. A., Bowyer S., Lea S. M., Pravdo S., 1981, *ApJ*, **247**, 803
- Reid A. D., Hunstead R. W., Lemonon L., Pierre M. M., 1999, *MNRAS*, **302**, 571
- Sanders J. S., Fabian A. C., Smith R. K., 2011, *MNRAS*, **410**, 1797
- Scaife A. M. M., Oozeer N., de Gasperin F., Brügger M., Tasse C., Magnus L., 2015, *MNRAS*, **451**, 4021
- Schwope A., et al., 2000, *Astronomische Nachrichten*, **321**, 1
- Shakouri S., Johnston-Hollitt M., Pratt G. W., 2016, *MNRAS*, **459**, 2525
- Shimwell T. W., Brown S., Feain I. J., Feretti L., Gaensler B. M., Lage C., 2014, *MNRAS*, **440**, 2901
- Shimwell T. W., Markevitch M., Brown S., Feretti L., Gaensler B. M., Johnston-Hollitt M., Lage C., Srinivasan R., 2015, *MNRAS*, **449**, 1486
- Sivanandam S., Zabludoff A. I., Zaritsky D., Gonzalez A. H., Kelson D. D., 2009, *ApJ*, **691**, 1787
- Slee O. B., Reynolds J. E., 1984, *Proceedings of the Astronomical Society of Australia*, **5**, 516
- Slee O. B., Roy A. L., 1998, *MNRAS*, **297**, L86
- Slee O. B., Roy A. L., Murgia M., Andernach H., Ehle M., 2001, *AJ*, **122**, 1172
- Sommer M. W., Basu K., 2014, *MNRAS*, **437**, 2163
- Srinivasan R., 2015, Master’s thesis, Victoria University of Wellington
- Struble M. F., Rood H. J., 1999, *ApJS*, **125**, 35
- Tingay S. J., et al., 2013, *PASA*, **30**, 7
- Tonry J. L., et al., 2012, *ApJ*, **750**, 99
- Trümper J., 1984, *Physica Scripta Volume T*, **7**, 209
- Vacca V., Govoni F., Murgia M., Giovannini G., Feretti L., Tugnoli M., Verheijen M. A., Taylor G. B., 2011, *A&A*, **535**, A82
- Valtchanov I., Murphy T., Pierre M., Hunstead R., Lémonon L., 2002, *A&A*, **392**, 795
- Venturi T., Bardelli S., Dallacasa D., Brunetti G., Giacintucci S., Hunstead R. W., Morganti R., 2003, *A&A*, **402**, 913
- Venturi T., Giacintucci S., Brunetti G., Cassano R., Bardelli S., Dallacasa D., Setti G., 2007, *A&A*, **463**, 937
- Venturi T., Giacintucci S., Dallacasa D., Cassano R., Brunetti G., Bardelli S., Setti G., 2008, *A&A*, **484**, 327
- Venturi T., Giacintucci S., Dallacasa D., Cassano R., Brunetti G., Macario G., Athreya R., 2013, *A&A*, **551**, A24
- Voges W., et al., 1999, *A&A*, **349**, 389
- Way M. J., Quintana H., Infante L., 1997, preprint, ([arXiv:astro-ph/9709036](https://arxiv.org/abs/astro-ph/9709036))
- Wayth R. B., et al., 2015, *PASA*, **32**, 25
- Wayth R. B., et al., 2018, *PASA*, **35**, 33
- Wen Z. L., Han J. L., 2013, *MNRAS*, **436**, 275
- White D. A., 2000, *MNRAS*, **312**, 663
- Wilson W. E., et al., 2011, *MNRAS*, **416**, 832
- Xie C., et al., 2020, *A&A*, **636**, A3
- Zaritsky D., Gonzalez A. H., Zabludoff A. I., 2006, *ApJ*, **638**, 725
- de Gasperin F., van Weeren R. J., Brügger M., Vazza F., Bonafede A., Intema H. T., 2014, *MNRAS*, **444**, 3130
- de Gasperin F., Intema H. T., van Weeren R. J., Dawson W. A., Golovich N., Wittman D., Bonafede A., Brügger M., 2015, *MNRAS*, **453**, 3483
- van Haarlem M. P., et al., 2013, *A&A*, **556**, A2
- van Weeren R. J., Brügger M., Röttgering H. J. A., Hoeft M., Nuza S. E., Intema H. T., 2011, *A&A*, **533**, A35
- van Weeren R. J., et al., 2013, *ApJ*, **769**, 101
- van Weeren R. J., et al., 2014, *ApJ*, **781**, L32
- van Weeren R. J., de Gasperin F., Akamatsu H., Brügger M., Feretti L., Kang H., Stroe A., Zandanel F., 2019, *Space Sci. Rev.*, **215**, 16
- van der Walt S., Colbert S. C., Varoquaux G., 2011, *Computing in Science & Engineering*, **13**, 22

A. Clusters with radio haloes

Table 7 Clusters known to host radio haloes as of July 2017 used in Section 4.2.1.

Cluster	z	S_{ν} ^a (mJy)	ν (MHz)	α	$\log(P_{1.4}/W \text{ Hz}^{-1})$	References ^b
Abell 0523	0.1	72.0 ± 3.0	1400	-1.47 ± 0.30	24.28 ± 0.02	l/-
Abell 3562	0.04	20.0 ± 2.0	1400	-1.5 ± 0.1	22.88 ± 0.04	2/3
Abell 2061	0.078	16.9 ± 4.2	1400	-1.8 ± 0.3	23.43 ± 0.11	4/4
Abell 2065	0.084	32.9 ± 11.0	1400	-1.47 ± 0.30	23.78 ± 0.15	4/-
CL 1446+26	0.37	9.2 ± 0.5	1400	-1.47 ± 0.30	24.70 ± 0.05	5/-
Abell 0746	0.232	18.0 ± 4.0	1382	-1.47 ± 0.30	24.49 ± 0.10	6/-
Abell 0399	0.071	16.0 ± 2.0	1400	-1.47 ± 0.30	23.31 ± 0.06	7/-
Abell 3411	0.168	4.8 ± 0.5	1400	-1.47 ± 0.30	23.61 ± 0.05	8/-
Abell 2034	0.113	13.6 ± 1.0	1400	-1.47 ± 0.30	23.67 ± 0.03	5/-
Abell 2294	0.169	5.8 ± 0.5	1400	-1.47 ± 0.30	23.69 ± 0.04	5/-
Abell 0781	0.3	20.5 ± 5.0	1400	-1.47 ± 0.30	24.83 ± 0.11	9/-
Abell 2069	0.116	28.8 ± 7.2	1400	-1.47 ± 0.30	24.02 ± 0.11	4/-
Abell 2254	0.178	33.7 ± 1.3	1400	-1.47 ± 0.30	24.51 ± 0.03	a/-
Abell 0851	0.406	3.7 ± 0.3	1400	-1.47 ± 0.30	24.40 ± 0.06	5/-
RXC J0107.8+5408	0.106	55.0 ± 5.0	1382	-1.47 ± 0.30	24.21 ± 0.04	6/-
Abell 1351	0.322	39.6 ± 3.5	1400	-1.47 ± 0.30	25.19 ± 0.05	5/-
Abell 2218	0.175	4.7 ± 0.47	1400	-1.47 ± 0.30	23.64 ± 0.05	b/-
Abell 0209	0.206	16.9 ± 1.0	1400	-1.47 ± 0.30	24.36 ± 0.04	5/c
Abell 0401	0.073	17.0 ± 1.0	1400	-1.47 ± 0.30	23.36 ± 0.03	d/-
RXC J1514.9-1523	0.22	102.0 ± 9.0	327	-1.47 ± 0.30	24.27 ± 0.20	e/-
PSZ1 G108.18-11.53	0.335	6.8 ± 0.2	1380	-1.4 ± 0.07	24.45 ± 0.02	f/f
MACS J1752.0+4440	0.366	164.0 ± 13.0	323	-1.47 ± 0.30	25.00 ± 0.20	g/-
Abell 2142	0.09	18.3 ± 1.83	1400	-1.47 ± 0.30	23.59 ± 0.04	b/-
PSZ1 G216.60+47.00	0.382	21.0 ± 2.2	323	-1.47 ± 0.30	24.16 ± 0.20	h/-
RXC J1314.4-2515	0.243	10.3 ± 0.3	610	-1.47 ± 0.30	23.78 ± 0.11	c/-
PSZ1 G086.47+15.31	0.26	11.0 ± 1.2	323	-1.47 ± 0.30	23.47 ± 0.20	h/-
Abell 1689	0.183	11.7 ± 3.4	1200	-1.47 ± 0.30	23.98 ± 0.13	i/-
MACS J0553.4-3342	0.431	62.0 ± 5.0	323	-1.47 ± 0.30	24.76 ± 0.20	g/-
MACS J0417.5-1154	0.443	10.6 ± 1.0	1575	-1.72 ± 0.15	25.08 ± 0.05	j/j
El Gordo	0.87	29.0 ± 3.0	610	-1.2 ± 0.1	25.65 ± 0.06	k/k
Abell 0800	0.222	10.6 ± 0.8	1400	-1.47 ± 0.30	24.23 ± 0.04	l/-
Abell 2255	0.081	56.0 ± 3.0	1400	-1.47 ± 0.30	23.97 ± 0.03	m/-
Abell 1656 (Coma)	0.023	720.0 ± 130.0	1400	-1.34 ± 0.06	23.94 ± 0.08	n/n
Abell 1550	0.254	7.7 ± 1.6	1400	-1.47 ± 0.30	24.23 ± 0.09	l/-
Abell 2256	0.058	103.4 ± 1.1	1400	-1.8 ± 0.3	23.94 ± 0.01	o/p
Abell 0754	0.054	86.0 ± 4.0	1400	-1.5 ± 0.3	23.79 ± 0.02	d/d
Abell 1995	0.319	4.1 ± 0.7	1400	-1.47 ± 0.30	24.19 ± 0.08	5/-

^a Flux densities are converted to a radio power at 1.4 GHz using a measured α where available otherwise assuming an average spectral index of -1.47 ± 0.30 . For measured flux densities without an associated uncertainty, we assume 10%.

^b References are provided as 'reference for S_{ν} /reference for α '.

Table 8 continued.

Cluster	z	S_V (mJy)	ν (MHz)	α	$\log(P_{1.4})$	References
Abell 0545	0.154	23.0 ± 1.0	1400	-1.47 ± 0.30	24.20 ± 0.03	d/-
Abell 3888	0.153	27.6 ± 3.1	1400	-1.48 ± 0.14	24.27 ± 0.05	q/q
PLCK G147.3-16.6	0.65	7.3 ± 1.1	610	-1.47 ± 0.30	24.69 ± 0.14	r/-
Abell 0773	0.217	12.7 ± 1.3	1400	-1.47 ± 0.30	24.28 ± 0.05	a/-
MACS J0416.1-2403	0.396	1.6 ± 0.14	1500	-1.6 ± 0.5	24.08 ± 0.08	s/s
Abell 0520	0.203	34.4 ± 1.5	1400	-1.47 ± 0.30	24.65 ± 0.03	a/-
Abell 2319	0.056	328.0 ± 28.0	1400	-1.2 ± 0.3	24.39 ± 0.04	4/4
Abell 0521	0.248	5.9 ± 0.5	1400	-1.88 ± 0.07	24.13 ± 0.04	5/t
Abell 0665	0.182	43.1 ± 2.2	1400	-1.04 ± 0.02	24.61 ± 0.02	b/u
Abell 1758	0.28	3.9 ± 0.4	1400	-1.47 ± 0.30	24.03 ± 0.05	5/-
RXC J2003.5-2323	0.317	35.0 ± 2.0	1400	-1.32 ± 0.06	25.10 ± 0.03	v/v
PLCK G171.9-40.7	0.27	18.0 ± 2.0	1400	-1.84 ± 0.14	24.70 ± 0.05	w/w
Abell 1914	0.171	64.0 ± 3.0	1400	-1.91 ± 0.03	24.78 ± 0.02	d/x
Abell 1300	0.308	20.0 ± 2.0	1400	-1.28 ± 0.09	24.82 ± 0.04	y/z
Abell 0697	0.282	5.2 ± 0.5	1382	-1.64 ± 0.06	24.17 ± 0.04	6/6
CL 1821-643	0.299	11.9 ± 0.5	1665	-1.0 ± 0.1	24.61 ± 0.02	A/B
Abell 2219	0.228	81.0 ± 4.0	1400	-1.47 ± 0.30	25.14 ± 0.03	d/-
Abell 2744	0.307	57.0 ± 3.0	1400	-1.19 ± 0.11	25.26 ± 0.03	z/z
CL 0016+16	0.541	5.5 ± 0.55	1400	-1.47 ± 0.30	24.89 ± 0.07	b/-
MACS J1149.5+2223	0.544	1.2 ± 0.5	1450	-2.1 ± 0.3	24.39 ± 0.19	g/g
Abell 2163	0.203	155.0 ± 2.0	1400	-1.18 ± 0.04	25.28 ± 0.01	C/u
1E 0657 (Bullet)	0.296	24.7 ± 1.5	2100	-1.57 ± 0.05	25.18 ± 0.03	D/D
MACS J0717.5+3745	0.548	118.0 ± 5.0	1465	-1.27 ± 0.02	26.23 ± 0.02	E/E
PSZ1 G285.0-23.7	0.39	2.02 ± 0.25	1867	-1.47 ± 0.30	24.28 ± 0.08	F/-
ACT-CL J0256.5+0006	0.36	5.6 ± 1.4	610	-1.0 ± 0.9	24.03 ± 0.36	G/G
MACS J2243.3-0935	0.44	10.0 ± 2.0	610	-1.47 ± 0.30	24.39 ± 0.15	H/-
Triangulum Australis	0.051	130.0 ± 4.0	1328	-1.47 ± 0.30	23.88 ± 0.02	I/-

References: (0) Brown et al. (2011); (1) Girardi et al. (2016); (2) Venturi et al. (2003); (3) Giacintucci et al. (2005); (4) Farnsworth et al. (2013); (5) Giovannini et al. (2009b); (6) van Weeren et al. (2011); (7) Murgia et al. (2010); (8) van Weeren et al. (2013); (9) Govoni et al. (2011); (a) Govoni et al. (2001); (b) Giovannini & Feretti (2000); (c) Venturi et al. (2007); (d) Bacchi et al. (2003); (e) Giacintucci et al. (2011); (f) de Gasperin et al. (2015); (g) Bonafede et al. (2012); (h) Bonafede et al. (2015); (i) Vacca et al. (2011); (j) Parekh et al. (2017); (k) Lindner et al. (2014); (l) Govoni et al. (2012); (m) Govoni et al. (2005); (n) Kim et al. (1990); (o) Clarke & Ensslin (2006); (p) Bridle et al. (1979); (q) Shakouri et al. (2016); (r) van Weeren et al. (2014); (s) Ogrean et al. (2015); (t) Brunetti et al. (2008); (u) Feretti et al. (2004); (v) Giacintucci et al. (2009); (w) Giacintucci et al. (2013); (x) Komissarov & Gubanov (1994); (y) Reid et al. (1999); (z) Venturi et al. (2013); (A) Bonafede et al. (2014); (B) Kale & Parekh (2016); (C) Feretti et al. (2001); (D) Shimwell et al. (2014); (E) Bonafede et al. (2009); (F) Martinez Aviles et al. (2016); (G) Knowles et al. (2016); (H) Cantwell et al. (2016); (I) Scaife et al. (2015).